Update on the Investigation of Commercial Drying Cycles Using the Advanced Drying Cycle Simulator

Spent Fuel and Waste Disposition

Prepared for
US Department of Energy
Spent Fuel and Waste Science and Technology

R.J.M. Pulido, S.G. Durbin, R. W. Williams,
B. Baigas, G.T. Vice, G. J. Koenig,
R.E. Fasano, and A. Salazar III

Sandia National Laboratories
September 23, 2022
Milestone No. M2SF-22SN010203033
SAND2022-xxxx

DISCLAIMER

This information was prepared as an account of work sponsored by an agency of the U.S. Government. Neither the U.S. Government nor any agency thereof, nor any of their employees, makes any warranty, expressed or implied, or assumes any legal liability or responsibility for the accuracy, completeness, or usefulness, of any information, apparatus, product, or process disclosed, or represents that its use would not infringe privately owned rights. References herein to any specific commercial product, process, or service by trade name, trade mark, manufacturer, or otherwise, does not necessarily constitute or imply its endorsement, recommendation, or favoring by the U.S. Government or any agency thereof. The views and opinions of authors expressed herein do not necessarily state or reflect those of the U.S. Government or any agency thereof.

Prepared by
Sandia National Laboratories
Albuquerque, New Mexico 87185 and Livermore, California 94550

Sandia National Laboratories is a multimission laboratory managed and operated by National Technology and Engineering Solutions of Sandia, LLC, a wholly owned subsidiary of Honeywell International, Inc., for the U.S. Department of Energy's National Nuclear Security Administration under contract DE-NA0003525.

ABSTRACT

The purpose of this report is to document updates on the apparatus to simulate commercial vacuum drying procedures at the Nuclear Energy Work Complex at Sandia National Laboratories.

Validation of the extent of water removal in a dry spent nuclear fuel storage system based on drying procedures used at nuclear power plants is needed to close existing technical gaps. Operational conditions leading to incomplete drying may have potential impacts on the fuel, cladding, and other components in the system during subsequent storage and disposal. A general lack of data suitable for model validation of commercial nuclear canister drying processes necessitates well-designed investigations of drying process efficacy and water retention. Scaled tests that incorporate relevant physics and well-controlled boundary conditions are essential to provide insight and guidance to the simulation of prototypic systems undergoing drying processes.

This report documents a new test apparatus, the Advanced Drying Cycle Simulator (ADCS). This apparatus was built to simulate commercial drying procedures and quantify the amount of residual water remaining in a pressurized water reactor (PWR) fuel assembly after drying. The ADCS was constructed with a prototypic 17×17 PWR fuel skeleton and waterproof heater rods to simulate decay heat. These waterproof heaters are the next generation design to heater rods developed and tested at Sandia National Laboratories in FY20.

This report describes the ADCS vessel build that was completed late in FY22, including the receipt of the prototypic length waterproof heater rods and construction of the fuel basket and the pressure vessel components. In addition, installations of thermocouples, emissivity coupons, pressure and vacuum lines, pressure transducers, and electrical connections were completed. Preliminary power functionality testing was conducted to demonstrate the capabilities of the ADCS.

In FY23, a test plan for the ADCS will be developed to implement a drying procedure based on measurements from the process used for the High Burnup Demonstration Project. While applying power to the simulated fuel rods, this procedure is expected to consist of filling the ADCS vessel with water, draining the water with applied pressure and multiple helium blowdowns, evacuating additional water with a vacuum drying sequence at successively lower pressures, and backfilling the vessel with helium. Additional investigations are expected to feature failed fuel rod simulators with engineered cladding defects and guide tubes with obstructed dashpots to challenge the drying system with multiple water retention sites.

This page is intentionally left blank.

ACKNOWLEDGEMENTS

The authors would like to acknowledge the hard work and commitment of all contributors to the project. In particular, we would like to acknowledge the strong support and leadership of Ned Larson at the Department of Energy. Sylvia Saltzstein (SNL) and Geoff Freeze (SNL) are to be commended for their programmatic and technical guidance. We also thank Dominic Fascitelli and Victor Figueroa for their thorough technical reviews of this report.

We would like to express our gratitude for the hard work and dedication of our technologists that made the success of this project possible.

This page is intentionally left blank.

CONTENTS

Abstract iii

Acknowledgements v

List of Figures ix

List of Tables xi

Executive Summary xiii

Acronyms / Abbreviations xvii

1 Introduction 1
- 1.1 Objective 1
- 1.2 Prototypic Thermal-Hydraulics 1
- 1.3 Residual Water 3
- 1.4 High Burnup Demonstration 4
  - 1.4.1 Transient Vacuum Drying Data 4
  - 1.4.2 Gas Sampling 5
  - 1.4.3 Scaled Demonstration 6

2 ADCS Development 7
- 2.1 Development Objectives 7
- 2.2 Advanced Drying Cycle Simulator Overview 7
- 2.3 Fuel Assembly 9
- 2.4 Basket Design and Fabrication 11
- 2.5 Emissivity Coupons of Internal Components 13
- 2.6 Pressure Vessel and Test Setup 14
- 2.7 Instrumentation 19
  - 2.7.1 Thermocouples 19
  - 2.7.2 Pressure Measurement and Control 23
  - 2.7.3 Water Content Measurement 24
- 2.8 Power Control 28

3 Current ADCS Status 33
- 3.1 Final Construction 33
- 3.2 Power Functionality Testing 34
- 3.3 Future Work 36

4 References 37

Appendix A List of Thermocouples 39

This page is intentionally left blank.

LIST OF FIGURES

Figure E-1 Major components of the Advanced Drying Cycle Simulator. xiii
Figure E-2 Thermal response of the ADCS to the application of 2.0 kW. xiv
Figure E-3 Demonstration of power control for an operational test at 2.0 kW. xv
Figure 1-1 Water retention sites exhibited in *a)* a typical 17×17 PWR fuel assembly construction, *b)* a typical PWR guide thimble tube, and *c)* a burnable poison rod assembly (Figures 3.1-16, 4.2-8, and 3.1-26 in NRC, 2002). 2
Figure 1-2 Cross-sections showing *a*) portions of fuel from the High Burnup Demonstration Project cask represented by *b*) the Dashpot Drying Apparatus and *c*) the Advanced Drying Cycle Simulator (figure not to scale). 6
Figure 2-1 The Advanced Drying Cycle Simulator located inside the Cylindrical Boiling Facility. 8
Figure 2-2 Photo of 17×17 PWR skeleton taken during thermocouple installation. 9
Figure 2-3 Waterproof heater rod diagram. 10
Figure 2-4 PWR skeleton fully outfitted with waterproof heaters. 11
Figure 2-5 Basket fabrication including the welds on the tabs and slots on the basket corners as well as the weld mating the two halves of the basket together. 12
Figure 2-6 Completion of basket fabrication through application of machine press to maintain 90-degree corners on basket interior. 12
Figure 2-7 Mouse hole cut into basket to provide clearance for thermocouples. 13
Figure 2-8 *a*) Cladding and basket emissivity coupon strips shown outside the ADCS vessel at installation height. *b*) Closeup of a cladding (left) and basket emissivity coupon (right). 14
Figure 2-9 Photo of the ADCS pressure vessel taken during hydrostatic testing. The ADCS vessel is divided into lower and upper pressure vessels. 15
Figure 2-10 Photo of the sight glass welded onto the bottom flange of the ADCS. 15
Figure 2-11 Photo looking up at the standoff that fixes the position of the heater assembly and the basket within the ADCS. The view is from below the lower pressure vessel with the bottom flange removed. 16
Figure 2-12 *a*) Photo of the top of the siphon tube used for bulk filling and draining of water. *b*) Photo of the bottom of the siphon tube. *c*) Closeup photo of the bottom of the siphon tube after being cut. *d*) Borescopic photo of the siphon tube resting on the bottom flange. 17
Figure 2-13 Photo of the ADCS pressure vessel. 18
Figure 2-14 Diagram of ADCS pressure/vacuum system. 19
Figure 2-15 Diagram of heater assembly thermocouple locations. 20
Figure 2-16 Visualization of heater assembly quadrants and thermocouple placement on heater rods. 21
Figure 2-17 Diagram of basket thermocouple locations. 22
Figure 2-18 Diagram of ADCS pressure vessel thermocouple locations. 23
Figure 2-19 Mass spectrum of air showing the major peaks for nitrogen. 25

Figure 2-20 Hiden Analytical HPR-20 mass spectrometer system with a QIC dual-stage sampling head for measuring water content (Hiden Analytical Limited, 2018a).....26

Figure 2-21 Hiden Analytical HPR-30 mass spectrometer system with a QIC dual-stage sampling head for measuring water content (Hiden Analytical Limited, 2018b). 26

Figure 2-22 HPR-20 and HPR-30 sampling pressure ranges.....27

Figure 2-23 Linear regression of the raw water content measurements for determining the relative sensitivity factor for water in a helium background when calibrating the HPR-20 mass spectrometer with respect to the S8000 chilled mirror hygrometer. 28

Figure 2-24 Diagram of the power control setup for the ADCS. 29

Figure 2-25 *a*) Primary and secondary bus plates for "hot" electrical connection used to supply power to heater rods. *b*) Neutral strap on top-most grid spacer. *c*) Separate neutral strap on bottom nozzle and lower pressure vessel. 30

Figure 2-26 *a*) Kapton insulation to prevent shorting between heater rods and basket. *b*) "Hot" electrical connection and Kapton insulation on Monel rod washers. *c*) Neutral electrical connection from heater assembly through the basket. Note that electrical connections shown here are for testing purposes.....31

Figure 3-1 Final ADCS electrical configuration. The top flange is not installed in this image. 33

Figure 3-2 Installation of top flange. 33

Figure 3-3 Thermal response throughout the center of the ADCS fuel assembly at an applied power of 2.0 kW. 34

Figure 3-4 Demonstration of power control at 2.0 kW. 35

Figure 3-5 Histogram of power for a nominal setting of 2.0 kW.....35

LIST OF TABLES

Table 1-1 Elapsed times for the TN-32B water removal and backfill procedures from the HBDP (EPRI, 2019). 5

Table 2-1 List of power control equipment. 29

Table A-1 List of ambient thermocouples. 39

Table A-2 List of heater assembly thermocouples. 39

Table A-3 List of internal (Int.) thermocouples not attached to the heater assembly. 43

Table A-4 List of external (Ext.) thermocouples. 44

This page is intentionally left blank.

EXECUTIVE SUMMARY

Technical gaps exist in the understanding of the extent of water removal in a dry spent nuclear fuel storage system with commercial canister drying procedures (Hanson & Alsaed, 2019). Operational conditions leading to substantial amounts of residual water may have potential impacts on the fuel, cladding, and other components in the system, such as fuel degradation and cladding corrosion, embrittlement, and breaching. Additional information is needed on drying process efficacy to evaluate the potential impacts of water retention on long-term dry storage. Given the lack of data suitable for model validation of drying processes, carefully designed investigations that incorporate relevant physics and well-controlled boundary conditions are needed to supplement existing field data. Experimental components, methodology, and instrumentation are therefore under development for use in advanced studies of realistic drying operations conducted on surrogate spent nuclear fuel.

A pressure vessel was devised that incorporated prototypic-length pressurized water reactor (PWR) hardware to demonstrate operational capabilities and the utilization of moisture monitoring equipment during drying processes as shown in Figure E-1. The Advanced Drying Cycle Simulator (ADCS) consists of a single PWR fuel assembly skeleton, a prototypic-length basket, a pressure/vacuum vessel, and waterproof heaters to simulate decay heat. The waterproof heaters were developed and tested at a reduced scale in FY20 and were subsequently scaled up to prototypic length for the ADCS.

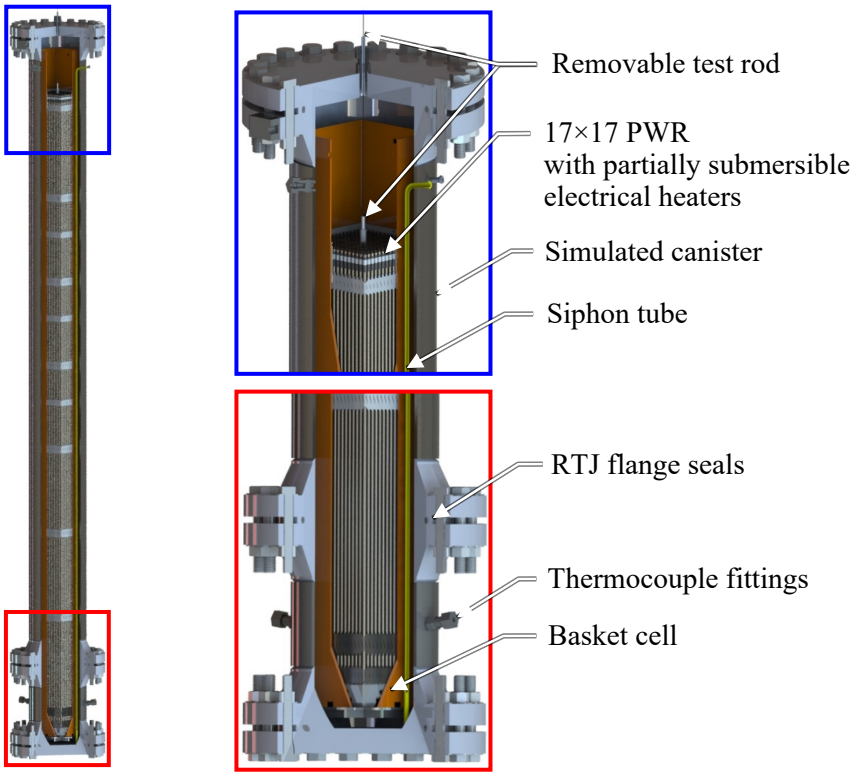

Figure E-1 Major components of the Advanced Drying Cycle Simulator.

FY22 efforts focused primarily on completion of the ADCS build, including the receipt of the prototypic-length waterproof heater rods and the construction of the basket and pressure vessel components. Also, installation of thermocouples, emissivity coupons, pressure and vacuum lines, pressure transducers, and electrical connections were finished. Preliminary functionality testing was conducted to demonstrate the capabilities of the ADCS.

Figure E-2 shows the results of an operational test of the ADCS heaters at an applied power of 2.0 kW. The M15 thermocouple (TC) is shown instead of J9 due to an apparent failure of the TC at that location. Based on the performance of the system during this operational test, the apparatus is expected to be capable of reproducing the heat-up observed in the High Burnup Demonstration Project (EPRI, 2019).

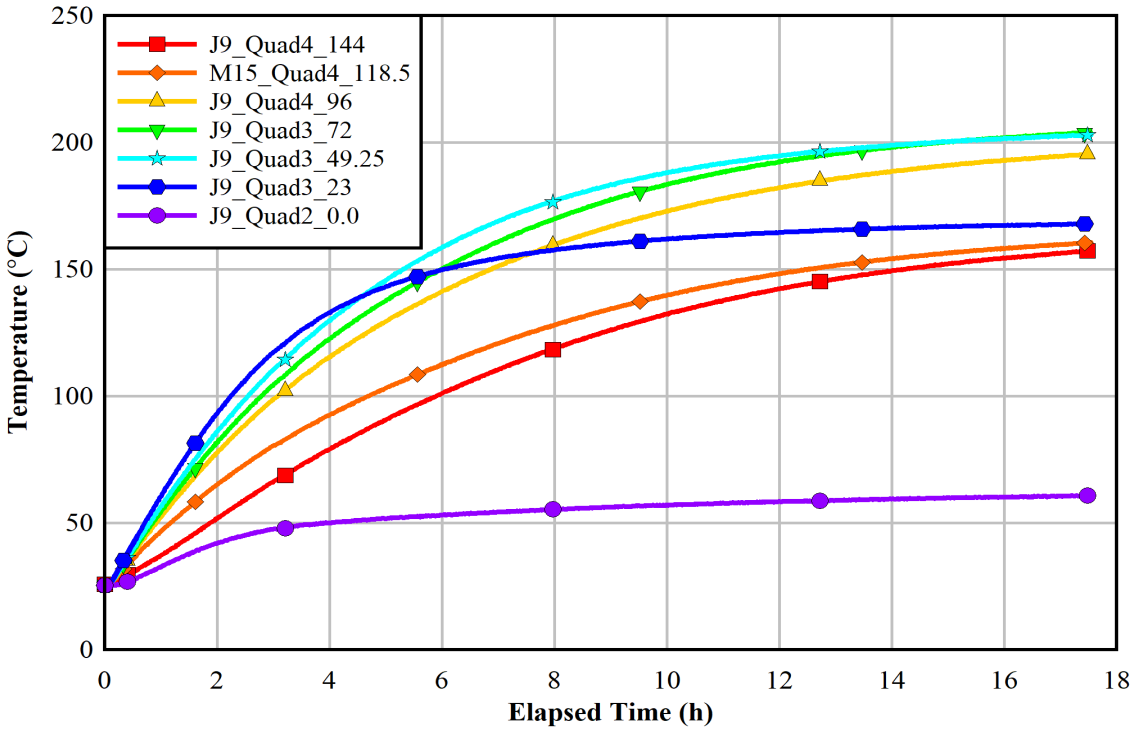

Figure E-2 Thermal response of the ADCS to the application of 2.0 kW.

Figure E-3 shows the corresponding power, voltage, and current from the 2.0 kW operational test. The average and standard deviation of the power were 2,004 and 8 W, respectively. This level of power control is acceptable, but additional improvements are planned. The data from this operational test offer confidence that the apparatus is viable and has plenty of margin to accomplish a wide array of drying tests. Pressure and vacuum leak tests will be completed next. Plumbing of the mass spectrometers and bulk water system will be the last components added to the system.

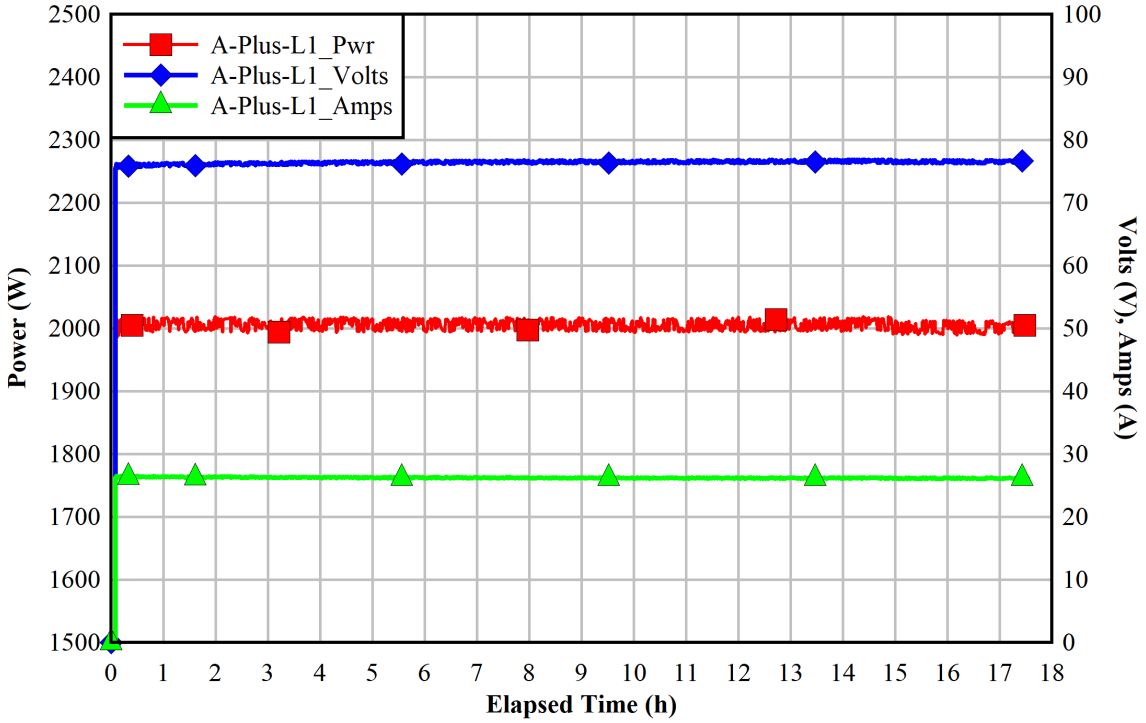

Figure E-3 Demonstration of power control for an operational test at 2.0 kW.

For future integrated testing, a drying procedure will be implemented based on measurements from the High Burnup Demonstration Project to investigate the efficacy of residual water removal after introduction and draining of water from the pressure vessel. Two mass spectrometers with specially designed inlets ("HPR-20" and "HPR-30") will be used to monitor moisture and gas composition across a continuous pressure range from 0.5 to 850 kPa (4 to 6,380 Torr), while other water removal behavior will be deduced from pressure and temperature measurements. Future experiments will feature a specialized test rod to introduce additional water retention sites that simulate the effects of failed fuel and crud as well as internal rod pressure monitoring. The insight gained through these investigations is expected to support the technical basis for the continued safe storage of spent nuclear fuel into long term operations.

This page is intentionally left blank.

ACRONYMS / ABBREVIATIONS

ADCS	Advanced Drying Cycle Simulator
DAQ	data acquisition system
DDA	Dashpot Drying Apparatus
DOE	Department of Energy
EPRI	Electric Power Research Institute
FHD	forced helium dehydration
FS	full-scale
GT	guide tube
HBDP	High Burnup Demonstration Project
ID	inner diameter
ISFSI	Interim Spent Fuel Storage Installation
MS	mass spectrometer
NE	Office of Nuclear Energy
NIST	National Institute of Standards and Technology
OD	outer diameter
ppmv	parts per million by volume
PV	pressure vessel
PWR	pressurized water reactor
SCR	silicon-controlled rectifier
SNF	spent nuclear fuel
SNL	Sandia National Laboratories
SFWD	Spent Fuel and Waste Disposition
SFWST	Spent Fuel and Waste Science and Technology
TC	thermocouple
VCR	vacuum coupling radiation
WVIA	water vapor isotope analyzer

This page is intentionally left blank.

UPDATE ON THE INVESTIGATION OF COMMERCIAL DRYING CYCLES USING THE ADVANCED DRYING CYCLE SIMULATOR

This report fulfills milestone report M2SF-22SN010203033 in the Spent Fuel and Waste Science and Technology (SFWST) work package (SF-22SN01020303). This work was sponsored under the Department of Energy's (DOE) Office of Nuclear Energy (NE) Spent Fuel and Waste Disposition (SFWD) campaign.

1 INTRODUCTION

1.1 Objective

Numerous water retention sites may exist within the internal volume of a multi-assembly dry storage system that require a specialized approach for the evacuation of water. While guidelines exist on ensuring sufficient evacuation of water from assembly cavities, there is a lack of time-dependent data on water removal from full-scale commercial drying procedures. Obtaining such data has been identified as a high-priority research topic to advance the technical basis for the long-term management of spent nuclear fuel (SNF) (Hanson and Alsaed, 2019). Operational conditions leading to incomplete drying may have potential impacts on the fuel, cladding, and other components in the system.

Drying procedures have been simulated in the laboratory (Colburn, 2022; Knight, 2019) and data has been obtained from samples of canisters subjected to commercial drying processes (Bryan *et al.*, 2019). While transient vacuum drying data has been analyzed for two small-scale apparatuses in previous studies at Sandia National Laboratories (SNL) (Salazar *et al.*, 2020; Durbin *et al.*, 2021; Pulido *et al.*, 2022), additional information is needed to evaluate the potential impacts of water retention on extended long-term dry storage for a commercial cask system. This includes unique locations in prototypic fuel assembly and canister hardware where water may be more difficult to remove, such as dashpots. Direct measurement of residual water in scaled systems representative of commercial canisters is therefore necessary to advance the current technical understanding of the drying procedures used by industry.

This report documents tests conducted on a single, simulated PWR assembly with prototypic geometry in a simplified vessel with well-controlled boundary conditions, known as the Advanced Drying Cycle Simulator (ADCS). This chapter will discuss the motivating issues underlying the investigation and a summary of past tests that were designed to respond to some of these concerns. Chapter 2 will discuss the development of the instrumentation, equipment, and procedures for the test series, including moisture-monitoring equipment. Chapter 3 will discuss the results of the ADCS functionality testing and future work.

1.2 Prototypic Thermal-Hydraulics

Prototypic hardware is incorporated to mimic the important geometries found in dry storage systems. One goal of this testing is to preserve actual fuel assembly geometry and associated retention sites for residual water.

Figure 1-1 shows locations within a PWR fuel assembly that can serve as water retention sites, such as the mixing vanes and bulge joints of the grid spacers. The fuel assembly features guide thimble tubes for the insertion of control rods or burnable poison assemblies which function as neutron absorbers for criticality control in the reactor. The dashpots in the guide tubes are designed to drain water through a centrally located through-hole in the guide thimble screw (i.e., vent hole). If the vent hole is fouled during reactor operations or pool storage, the dashpot could conceivably retain bulk water during the initial draining operations preceding canister drying. However, the water would be free to communicate with the interior of the canister via the flow holes and the open top of the guide thimble tube during drying operations.

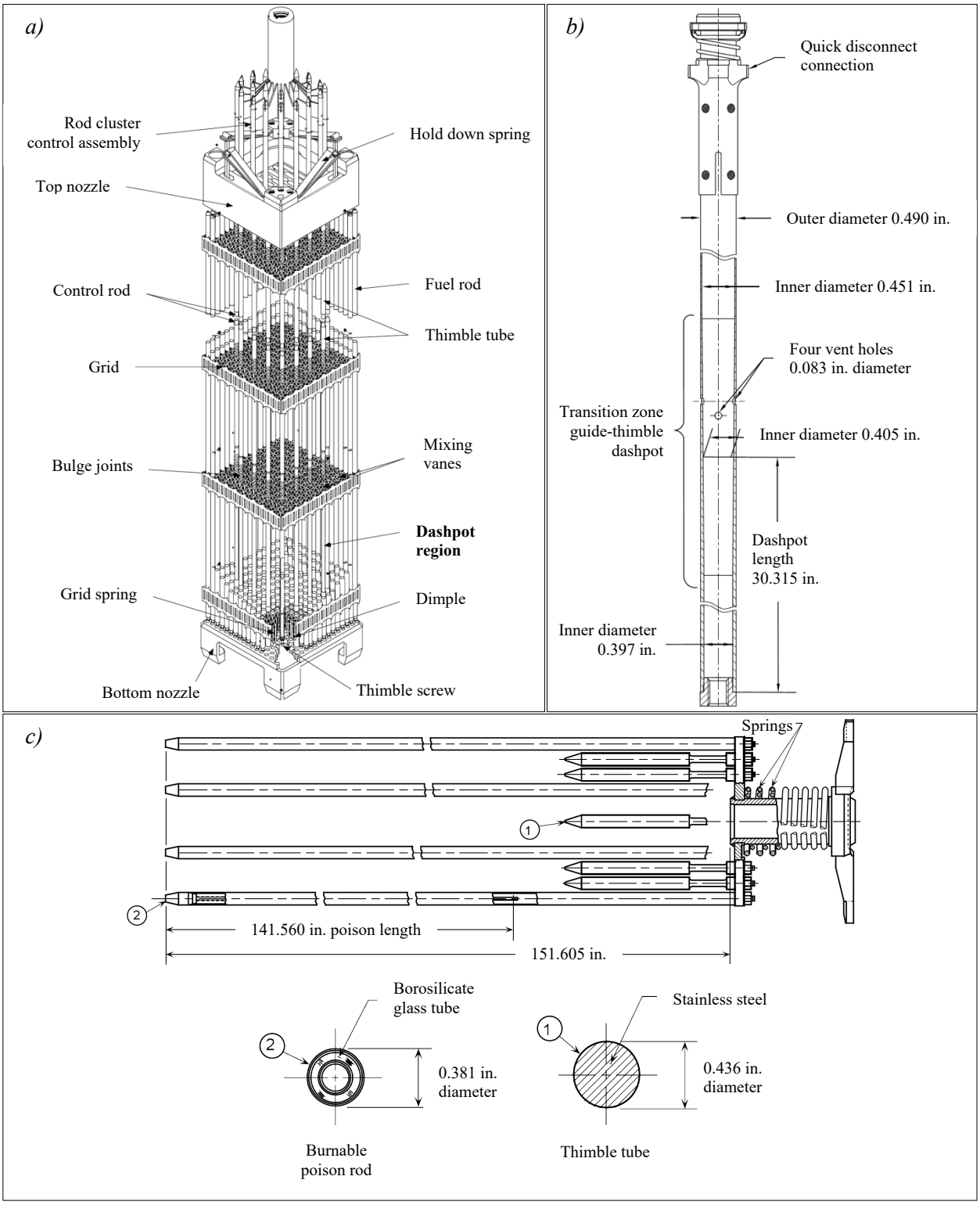

Figure 1-1 Water retention sites exhibited in *a)* a typical 17×17 PWR fuel assembly construction, *b)* a typical PWR guide thimble tube, and *c)* a burnable poison rod assembly (Figures 3.1-16, 4.2-8, and 3.1-26 in NRC, 2002).

Burnable poison rods are inserted and left in some fuel assemblies, which could restrict the flow area for any trapped water in the dashpot region if the vent hole is fouled.

1.3 Residual Water

Spent fuel assemblies are dried after interim storage in pools to ensure the removal of water in assembly cavities as a defense against issues related to pressurization and corrosion that might occur during the subsequent, potentially long-term, dry storage process. The evacuation of most water and oxidizing agents contained within the canister is recommended by NUREG-2215 (NRC, 2020). A pressure of 0.4 kPa (3 Torr) is recommended to be held in the canister for at least 30 minutes while isolated from active vacuum pumping as a measure of sufficient dryness in the canister. A similar drying method developed at Pacific Northwest National Laboratory (PNNL) is suggested (Knoll & Gilbert, 1987), where less than 0.25 volume percent (2500 ppm_v) of oxidizing gases are left in the canister (1 mole in 7 m^3 at 150 kPa and 300 K).

An industry standard guide was established for the drying of SNF after cooling in spent fuel pools (ASTM, 2016). The main purpose of the standard is to aid in the selection of a drying system and a means of ensuring that adequate dryness is attained. Examples of typical commercial processes are documented in the standard, where there is adherence to the aforementioned 0.4 kPa (3 Torr) level when discussing the measurement of pressure rebounds during system isolation from the vacuum pump. However, there are no substantial details on the utilization of moisture content measurements to ensure adequate water removal, and the establishment of related dryness metrics are deferred to regulatory agencies. There is only a broad recommendation to impose drying conditions that maximize moisture removal from the system.

Water remaining in canisters upon completion of vacuum drying can lead to corrosion of cladding and fuel, embrittlement, and breaching. There is also some risk of creating a flammable environment from free hydrogen and oxygen generated via the radiolysis of water. The remnant water may be chemically absorbed (chemisorbed), physically absorbed (physisorbed), frozen, or otherwise trapped in cavities, blocked vents, breached clads, damaged fuel, etc. Chemisorbed water is bound to components by forces equivalent to a chemical bond, such as the formation of hydroxides and hydrates on zirconium, or corrosion products on the fuel or cladding. Physisorbed water is bound to components by weaker forces (e.g., Van der Waals, capillary) as an adsorbate, and increased surface area provided by material defects enhances this effect.

The removal of unbound water is largely dependent on the geometry and tortuosity of the components and the speed of the drying process. Cladding breaches are notable cases in that water can become trapped inside a fuel rod between fuel pellets and absorbed in cracks and voids. Water vapor may continue to be diffusively released after vacuuming. Depending on the thermal profile, condensation may occur on the cooler surfaces of the canister and internal hardware, such as those lying at the lower extremes distant from heat emitting SNF.

The pressure applied during vacuum drying lies below the water vapor pressure. Given the unique heat retention and phase change properties of water, when significant heat is removed during volatilization, some quantity of liquid may freeze (ASTM, 2016) and inhibit water removal. It is therefore important to understand under what marginal conditions ice may form during the procedure. Careful control of the vacuum pumps may prevent ice formation by controlling suction near pressures liable to introduce liquid-to-solid phase transitions. Further mitigation may be achieved by implementing pressure reduction in stages that involve bringing the temperature to equilibrium with hot inert gases like helium prior to commencement of the next stage. In a general expansion of this concept, further research and development on forced helium dehydration (FHD) has been recommended to address recently identified technological gaps (Hanson & Alsaed, 2019).

If vacuum is employed to remove water from a canister, measurements in the pressure response to intermittent pump operation may serve as a good indicator of residual, unbound water (ASTM, 2016).

Such an approach would involve analysis of the time-dependent pressure rebound when the vacuum pump is isolated from the system. The system is considered adequately dry if the system pressure remains below 0.4 kPa (3 Torr) for at least 30 minutes. Monitoring the moisture content in gas removed from the canister is also suggested as a means of evaluating adequate dryness. Dew point monitoring and spectroscopic techniques could be used to this end, although these measurements must be benchmarked to understand how they scale to various levels of dryness.

1.4 High Burnup Demonstration

The High Burnup Demonstration Project (HBDP) spent fuel data project from the DOE SFWST program is an ongoing research platform to examine the performance of high burnup SNF in dry storage systems. The project included the loading, drying, and storage of an Orano TN-32B cask at the Independent Spent Fuel Storage Installation (ISFSI) at the North Anna Nuclear Power Station in Virginia.

1.4.1 Transient Vacuum Drying Data

Data are available on the drying procedures employed in the transfer of the assemblies to the decontamination bay and subsequent loading into the TN-32B (EPRI, 2019) along with STAR-CCM+ and COBRA-SFS model validation (J. Fort *et al*., 2019). These data include ambient temperatures at the facilities, cask surface temperatures, and fuel temperatures, along with additional measurements for long-term cask monitoring. Of particular importance to this report are the data obtained and analyzed for the transients observed during the loading and vacuum drying processes. That is, time-dependent measurements from the HBDP are poised to inform the test setup for this scaled demonstration with prototypic hardware.

The SNF within the TN-32B was put through a prototypic loading and drying process with some minor exceptions involving the installation of instrumentation. The process proceeded as follows:

1. Loading of SNF assemblies from the spent fuel pool into the submerged cask.
2. Movement of the cask into the decontamination bay and installation of the draining and drying equipment.
3. Drainage of the cask using helium as a cover gas.
4. Multiple blowdowns of the cask until bulk flow of liquid water was visually observed to cease.
5. Vacuum drying of the cask using successive stages of increasingly low pressures until the pressure was observed to not exceed 3 Torr within 30 minutes when the cask was isolated.
6. Backfilling of the canister with helium to 222 kPa (1665 Torr).

For the scaled test, the simulation capability of the experimental apparatus can accommodate water filling (representing the cask loading within the pool and the transfer period), drainage, blowdown, vacuum drying, and backfilling. Table 1-1 shows the elapsed times for major events during the HBDP drying processes starting with the beginning of the water draining. This sequence of events, and the resulting temperatures and pressures in the fuel and cask, sets the values for which the ADCS tests are planned to replicate.

The peak measured temperature during vacuum drying was 237 °C, which occurred at the center of the cask slightly above the mid-plane eight hours after the start of vacuum drying (EPRI, 2019). Due to the offset of the thermocouple lance, this maximum implied a peak cladding temperature of 240 °C, which is well below the regulatory limit of 400 °C. The maximum steady-state measurement of 231 °C was obtained during the helium backfill. The maximum external cask surface temperature was 88.3 °C near the cask midplane as measured 12 days after the backfill with helium.

Table 1-1 Elapsed times for the TN-32B water removal and backfill procedures from the HBDP (EPRI, 2019).

Procedure	Elapsed Time (h)
Begin drain	0.00
Finish drain	0.72
Begin blowdowns	4.63
Finish blowdowns	7.18
Begin vacuum drying	7.22
Vacuum drying complete	14.31
Begin initial helium backfill	15.63
Begin final helium backfill	16.22
Finish backfill	17.03

1.4.2 Gas Sampling

Prior to transportation to the ISFSI, samples of the helium backfill gas were collected at 5 hours, 5 days, and 12 days after the drying process (Bryan *et al.*, 2019). Samples were obtained in 1 L cylinders pressurized to 20 psig. Gas samples were analyzed first at room temperature by Dominion Energy using a gas chromatograph. They were then re-analyzed in a more thorough manner with heating at SNL to mitigate sorption effects in the sample bottles. Mass spectrometry was used to quantify bulk and trace gases in the sample while a humidity sensor was used to measure water content.

The Dominion water content analysis employed a Los Gatos Research Water Vapor Isotope Analyzer (WVIA). The instrument is designed for ambient vapor analysis in the field using an absorption technique with an optical cavity measurement cell. Although it operates best with a continuous flow stream, the North Anna cask could not be sampled directly as a failure scenario would result in a release pathway to the decontamination bay. Therefore, the static samples were employed instead and analyzed continuously while connected to the WVIA. The measured water content was 1633, 8896, and 8300 ppm_v for samples 1 through 3, respectively.

The mass spectrometer (MS) employed in the SNL analysis was a Finnigan MAT 271 high-resolution MS specialized for hydrogen isotope measurements via a stable gas ionization source. The instrument employs a combination Faraday cup and secondary electron multiplier for measurement of bulk and trace gases, respectively, and it was calibrated using a precision gas mixture. Measurements were obtained with a 50 cm^3 sample cylinder in line with a high vacuum system using an established high-purity sample and measurement procedure. Water was able to be measured, but its content was underestimated when present as a trace gas and overestimated when present in higher concentrations. Therefore, only estimates of the water content could be provided by the MS due to sorption effects in the sample chamber. However, valuable insight was gained on radiolysis and the formation of anoxic corrosion byproducts and hydrogen gas. Also, no fission gases were detected in the analyses, indicating a lack of fuel failure during cask loading.

The ultimate sensor used for water content measurement at SNL was a Vaisala model HMP77B relative humidity probe mounted to the sample bottle on a tee with a pressure gauge. With an operating range of -70 °C to 180 °C, the probe could be placed directly in an oven during sample heating. It was also capable of static measurements but valves in the vacuum line required some period of time for the system to re-settle for a given adjustment. Measurements were obtained at temperatures ramping up to 65 °C. Water content was found to be 10,000 $ppm_v \pm 1000$ ppm_v and 17,400 $ppm_v \pm 1740$ ppm_v five and twelve days after drying, respectively, ultimately indicating that 100 grams of water remained in the gas phase in the cask. (The measurements of the 5-hour sample were affected by a leak, but the room temperature measurement was 2097 ppm_v). However, because the relative humidity was less than the anticipated 10%

at 85 °C at the time of sampling, no liquid water was found to exist within the canister unless trapped in locations inaccessible to the drying system.

Given the method of sampling from the HBDP, it may not be possible to implement an MS or humidity probe in a canister with live SNF. Regulatory guidelines present limitations in the type of data that can be obtained in a commercial system. For example, it may not be possible to sample gas for mass spectrometry from the vacuum drying process using a slip stream.

1.4.3 Scaled Demonstration

Figure 1-2 shows conceptual vertical cross-sections through the HBDP cask, the Dashpot Drying Apparatus (DDA) tested in the first half of FY22 (Pulido *et al*., 2022) and the ADCS, which is the focus of this report. Figure 1-2a on the left is adapted from Figure 1.2-1 in TN-32 Final Safety Analysis Report (FSAR), Revision 2. Figure 1-2b shows the DDA, and Figure 1-2c shows the ADCS. The DDA, a small-scale drying apparatus, was built and tested to provide preliminary quantitative assessments of water content in the dashpot region of a PWR assembly. The ADCS scales the drying testing up to prototypic length and its construction will be described in detail in Chapter 2.

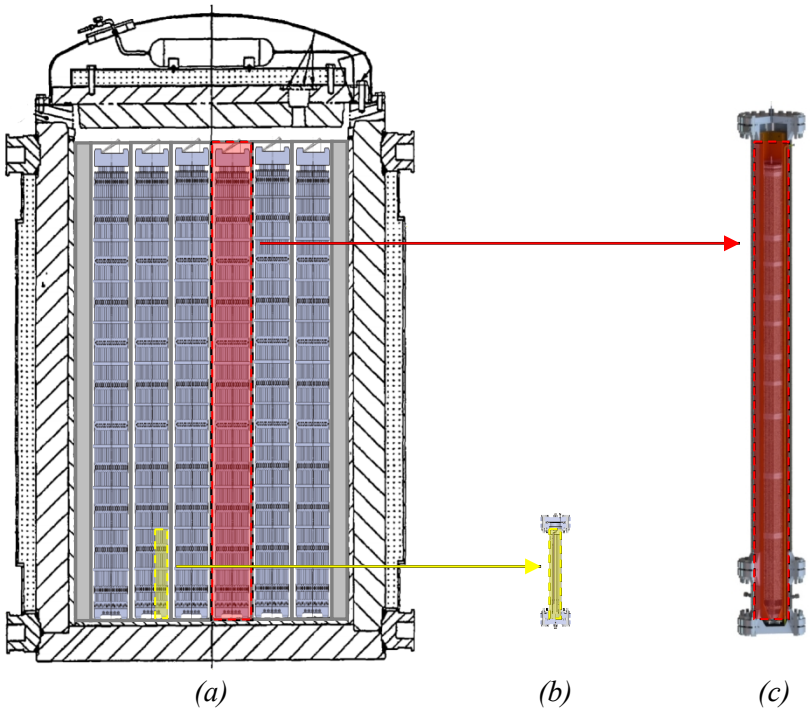

Figure 1-2 Cross-sections showing *a*) portions of fuel from the High Burnup Demonstration Project cask represented by *b*) the Dashpot Drying Apparatus and *c*) the Advanced Drying Cycle Simulator (figure not to scale).

2 ADCS DEVELOPMENT

This chapter will discuss the development of the ADCS testing setup that aims to address gaps in the current understanding of vacuum drying and residual water analysis that were previously covered in SAND2022-3813 R, "Response of a Pressurized Water Dashpot to Commercial Drying Cycles," (Pulido *et al.*, 2022), SAND2021-11828 R, "Update on the Simulation of Commercial Drying of Spent Nuclear Fuel," (Durbin *et al*., 2021), SAND2020-5341 R, "Development of Mockups and Instrumentation for Spent Fuel Drying Tests," (Salazar *et al.*, 2020) and SAND2019-11281 R, "Advanced Concepts for Dry Storage Cask Thermal-Hydraulic Testing" (Salazar *et al.*, 2019).

2.1 Development Objectives

FY22 developments focused on the construction of the Advanced Drying Cycle Simulator. This system allows for thermal-hydraulic investigations of drying efficiency with prototypic hardware. FY22 testing focused on ADCS functionality in preparation for the simulation of commercial drying procedures using prototypic hardware.

The main objectives of the development and testing include the following:

1. Complete construction and instrumentation of the Advanced Drying Cycle Simulator
2. Preliminary functionality testing of the ADCS through waterproof heater rod power testing and instrumentation testing

Performance verification in this test series with the ADCS will support more advanced drying tests. In turn, data can be provided that are readily scalable to commercial dry cask storage and transportation applications.

2.2 Advanced Drying Cycle Simulator Overview

The ADCS is a prototypic-length pressure vessel whose purpose is to simulate commercial drying cycles. It contains a simulated 17×17 PWR assembly, outfitted with waterproof heater rods and prototypic components (top and bottom nozzles, grid spacers, basket, siphon tube). The ADCS has been built inside of the Cylindrical Boiling (CYBL) facility at Sandia National Laboratories (SNL), as shown in Figure 2-1.

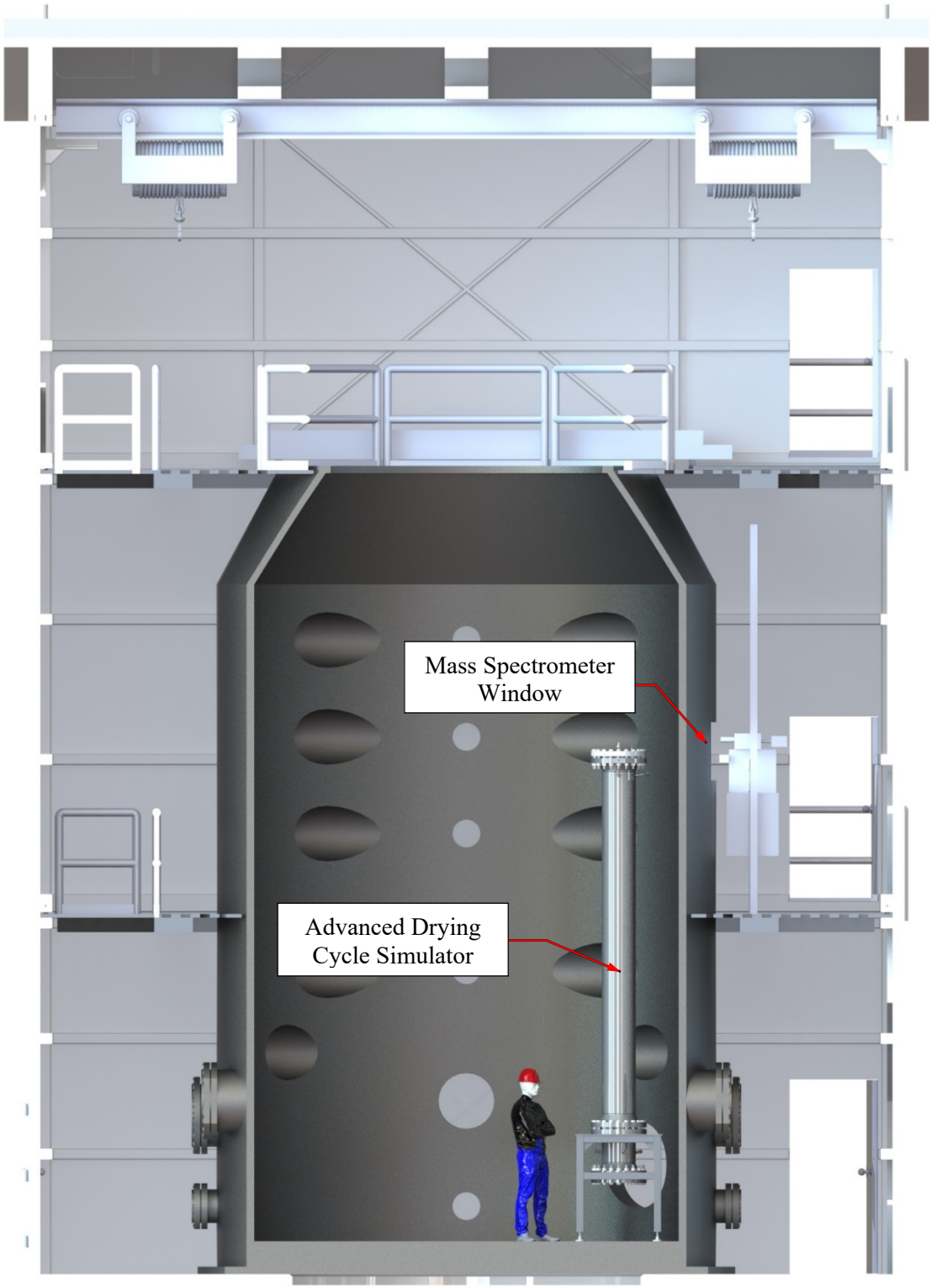

Figure 2-1 The Advanced Drying Cycle Simulator located inside the Cylindrical Boiling Facility.

2.3 Fuel Assembly

The fuel assembly was constructed using a 17×17 PWR skeleton. The PWR skeleton is made using prototypic hardware and thus contains representative geometries of interest for water retention. A photo taken during thermocouple (TC) installation on the skeleton is shown in Figure 2-2. More details on TC installation will be discussed in Section 2.7.1.

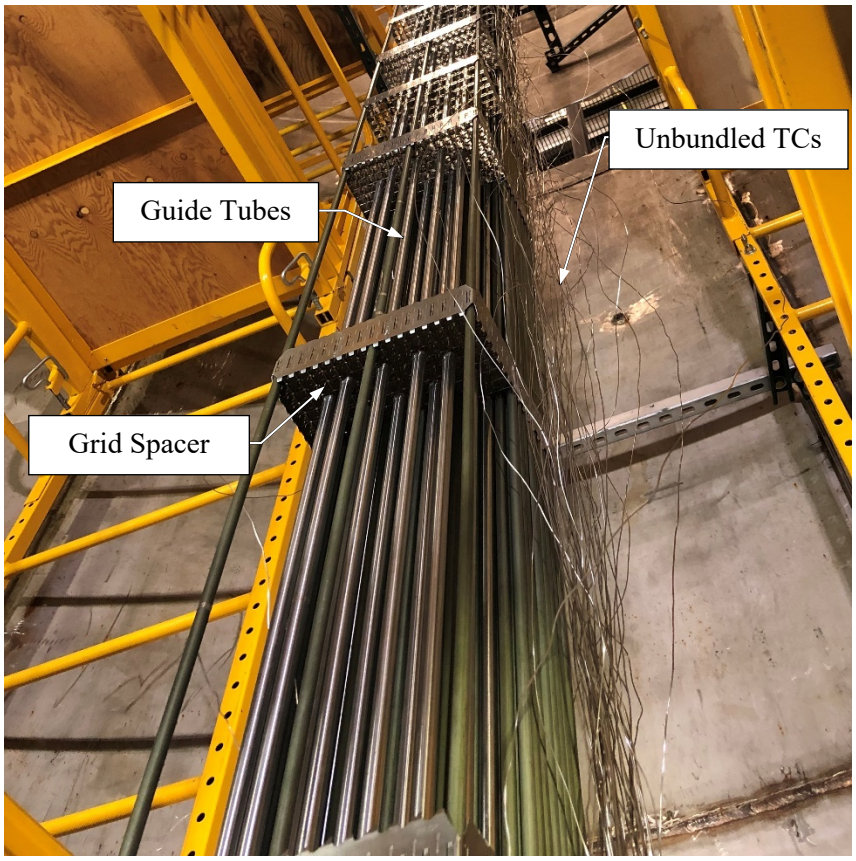

Figure 2-2 Photo of 17×17 PWR skeleton taken during thermocouple installation.

The skeleton was fully outfitted with waterproof heater rods. Initial development and testing of the heater rod design was completed in FY19 (Salazar *et al*., 2019) and extensive testing of the concept was conducted in FY20 (Salazar *et al*., 2020). The heater rod was demonstrated to fully perform while partially submerged under water as well as under pressurized, evacuated, and moist conditions (Salazar *et al.*, 2019). It was also observed to be unaffected by boiling water at atmospheric pressure, indicating that the electrically insulating material was not compromised by steam production or condensation reflux. These results confirmed the rod's candidacy for use in tests meant to assess thermal phenomena in a dynamic, wet environment expected during drying operations (Salazar *et al*., 2020). The conceptual diagram for the waterproof heater rod is shown in Figure 2-3 and the fully outfitted PWR skeleton is shown in Figure 2-4.

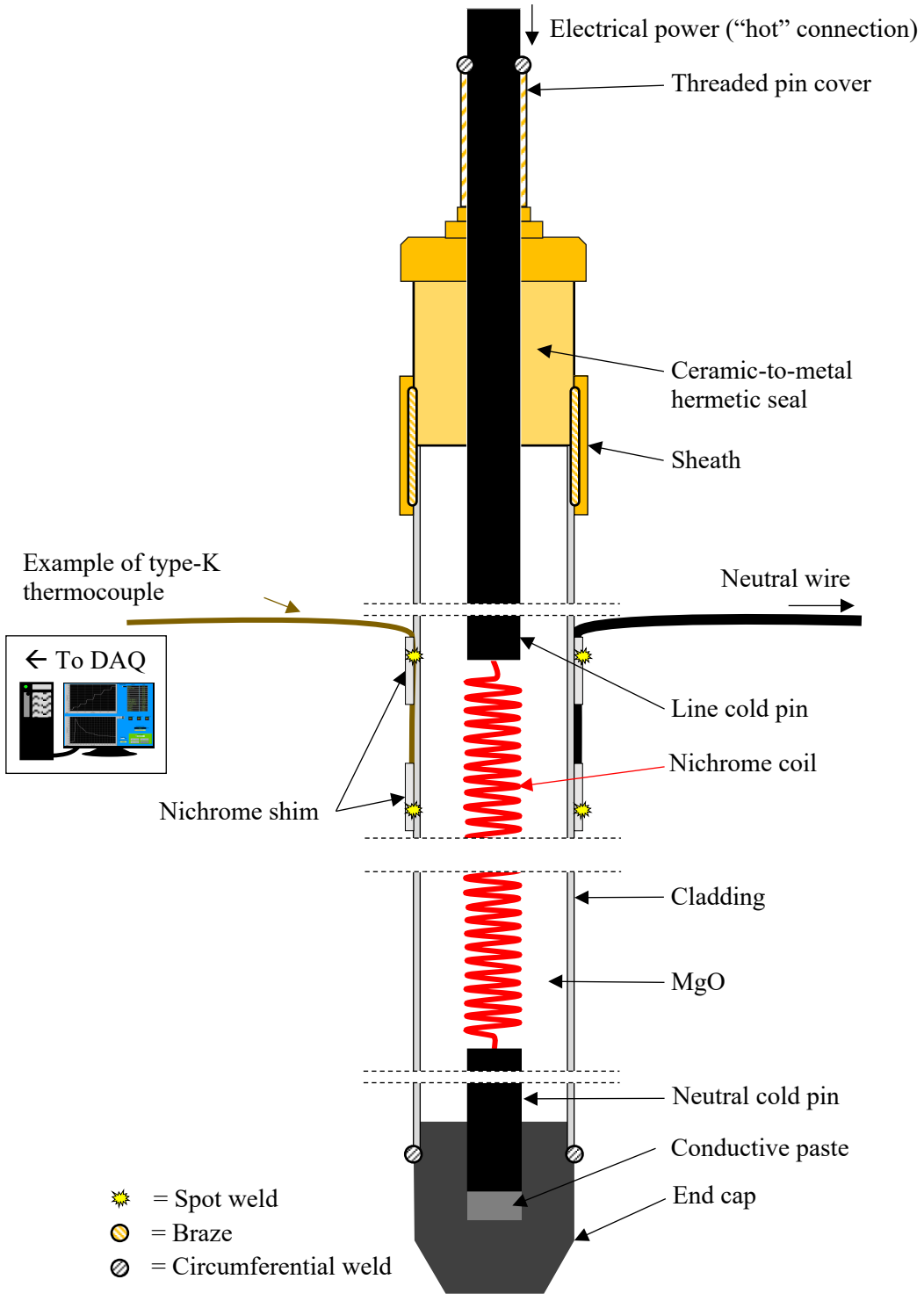

Figure 2-3 Waterproof heater rod diagram.

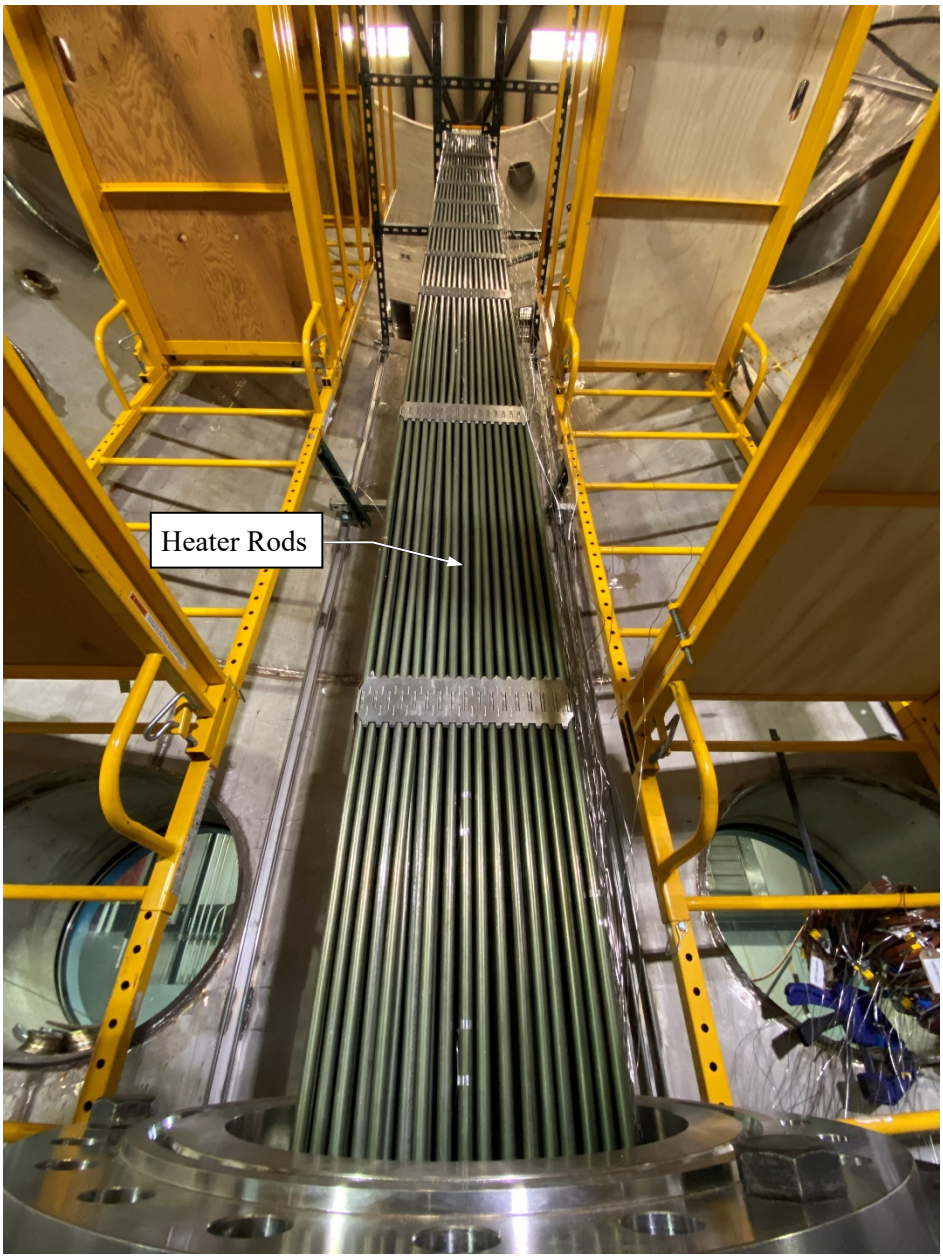

Figure 2-4 PWR skeleton fully outfitted with waterproof heaters.

2.4 Basket Design and Fabrication

The basket was designed and fabricated in-house using four 304 stainless steel sheet metal pieces bent into 90-degree angles. The sheet metal had tabs and slots machined along one edge, allowing two of the 90-degree pieces to come together and form a half-length basket by welding the tabs and slots together (see Figure 2-5). A weld along the basket's mid-point circumference mated the two half-basket pieces together as shown in Figure 2-5. A machine press was used to maintain the basket's shape after the tab and slot diagonal across the entire basket was welded for a seamless finish, as shown in Figure 2-6.

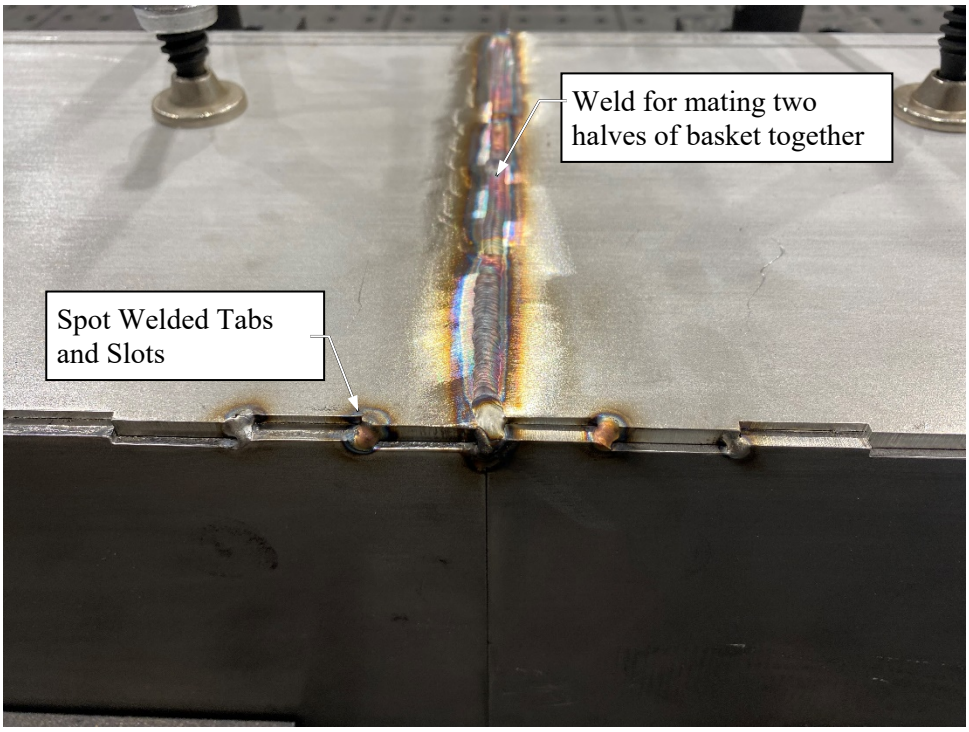

Figure 2-5 **Basket fabrication including the welds on the tabs and slots on the basket corners as well as the weld mating the two halves of the basket together.**

Figure 2-6 **Completion of basket fabrication through application of machine press to maintain 90-degree corners on basket interior.**

When lifting the basket over the heater rod assembly, it became apparent that the position of the basket would cause it to provide excess strain on the thermocouples due to the position of the TC fittings on the ADCS lower pressure vessel (see next section). Therefore, mouse holes were cut into three of the four sides of the basket to provide clearance for the thermocouples (see Figure 2-7).

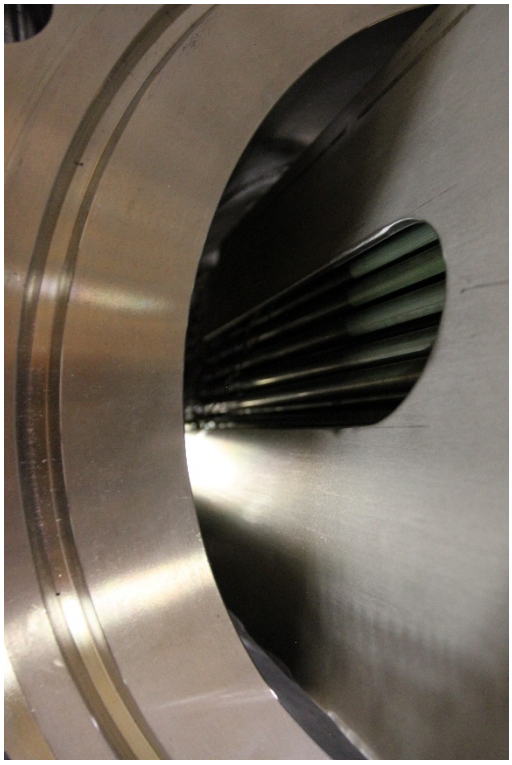

Figure 2-7 Mouse hole cut into basket to provide clearance for thermocouples.

2.5 Emissivity Coupons of Internal Components

Emissivity data from the heater cladding and fuel basket inside the ADCS are of particular interest to support model validation. This data is inherently difficult to obtain directly from these internal components, as they are inaccessible after assembly. To provide emissivity data for these components in an as-installed condition and to be able to measure emissivity changes over time, two emissivity coupon strips containing heater cladding and basket material at fixed intervals matching thermocouple locations within the ADCS were constructed and installed (details of those locations are given in Section 2.7.1). The emissivity coupon strips are shown in Figure 2-8. The approximate regions for the emissivity measurements are shown by dashed red circles in Figure 2-8b.

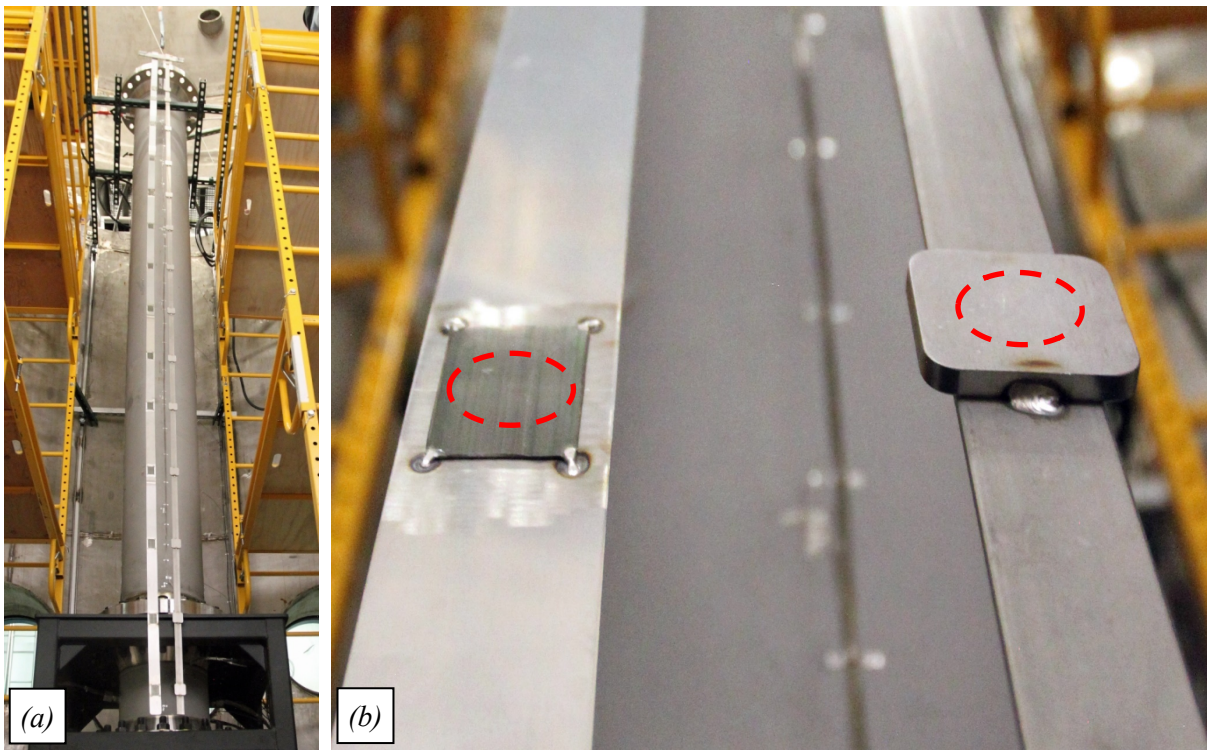

Figure 2-8 *a*) Cladding and basket emissivity coupon strips shown outside the ADCS vessel at installation height. *b*) Closeup of a cladding (left) and basket emissivity coupon (right).

The emissivity of the coupons was measured before insertion into the ADCS vessel to provide baseline emissivities for the heater cladding and fuel basket. At periodic intervals during testing, the coupon sheet will be extracted from the vessel, and emissivity measurements will be taken again to measure how the emissivity of the coupons has changed over time. The coupon strips will then be reinserted into the ADCS.

2.6 Pressure Vessel and Test Setup

A pressure vessel (PV) was constructed of nominal fourteen-inch 304/304L, dual-certification, stainless-steel schedule 40 pipe terminated with welded flanges. The flanges were connected to blinds by ring-type joints (RTJs). The entire ADCS vessel is split into upper and lower pressure vessels. Penetrations into the PV are made via welded glands with vacuum coupling radiation (VCR) face seal connections. Four penetrations are located on the lower pressure vessel and use Spectite fittings for the feedthrough of the TCs. Five penetrations are located on the upper pressure vessel – two use Conax fittings for the hot and neutral feedthroughs, two use 0.5-inch VCR fittings for the gas fill inlet and the siphon tube (details included later in this section), and one 0.25-inch VCR fitting for the vacuum pumps (details included later in this section). The top flange on the end of the upper pressure vessel contains a Conax fitting for a test rod as well as a 0.25-inch VCR fitting to be used as a sampling port for the mass spectrometers (details in Section 2.7.3). All VCR connections are sealed with unplated, non-retaining stainless-steel gaskets. The top and bottom flanges are sealed with stainless-steel octagonal ring-type gaskets.

A photo of the pressure vessel is shown in Figure 2-9. Hydrostatic testing of the pressure vessel, consisting of 30 minutes of exposure to water at 4,140 kPa (600 psia), was successful.

Figure 2-9 Photo of the ADCS pressure vessel taken during hydrostatic testing. The ADCS vessel is divided into lower and upper pressure vessels.

The bottom flange was modified to incorporate a sight glass, which was welded onto the flange for visual internal monitoring of the lower dashpot region of the PWR assembly. A photo of the sight glass is shown in Figure 2-10.

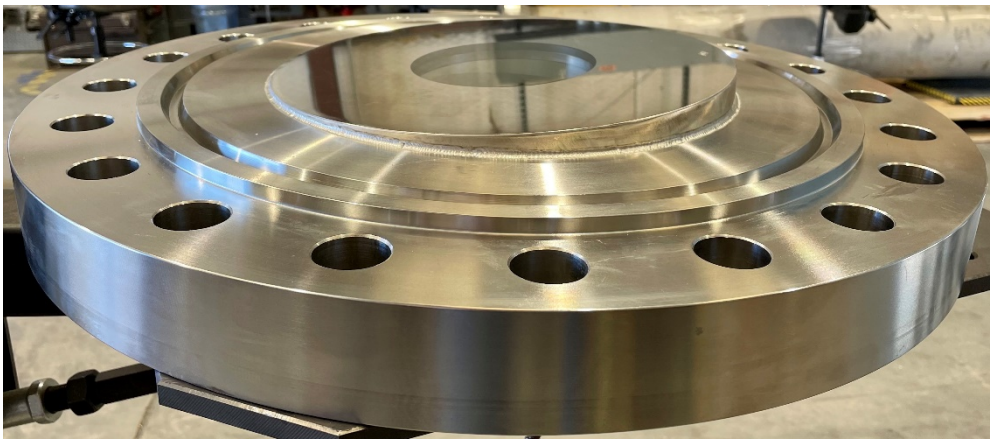

Figure 2-10 Photo of the sight glass welded onto the bottom flange of the ADCS.

The bottom of the lower pressure vessel was outfitted with a PWR standoff that is welded to the interior to support the fuel assembly and basket. This standoff is shown in Figure 2-11.

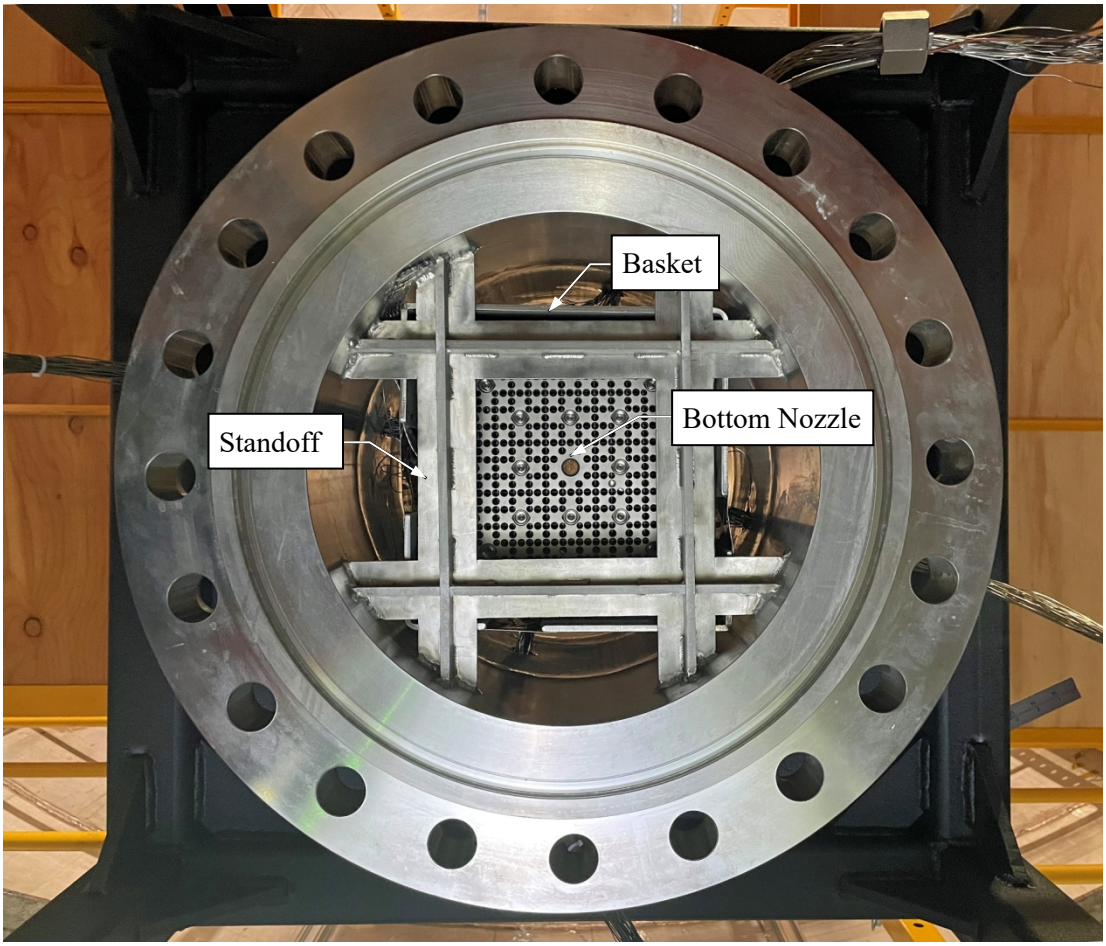

Figure 2-11 Photo looking up at the standoff that fixes the position of the heater assembly and the basket within the ADCS. The view is from below the lower pressure vessel with the bottom flange removed.

A siphon tube (0.402-inch ID, 0.5-inch OD, 316/316L stainless steel) was installed for bulk filling and draining of water and is representative of the hardware used during commercial drying. The siphon tube was positioned between the ADCS pressure vessel and basket and penetrates through to the ADCS exterior 161.8 inches above the top of the bottom nozzle. The tube was set in its position penetrating the pressure vessel as shown in Figure 2-12a. The tube was purposely oversized so it could be cut to the correct length and angle for positioning at the bottom of the pressure vessel just above the sight glass, as shown in Figure 2-12b.

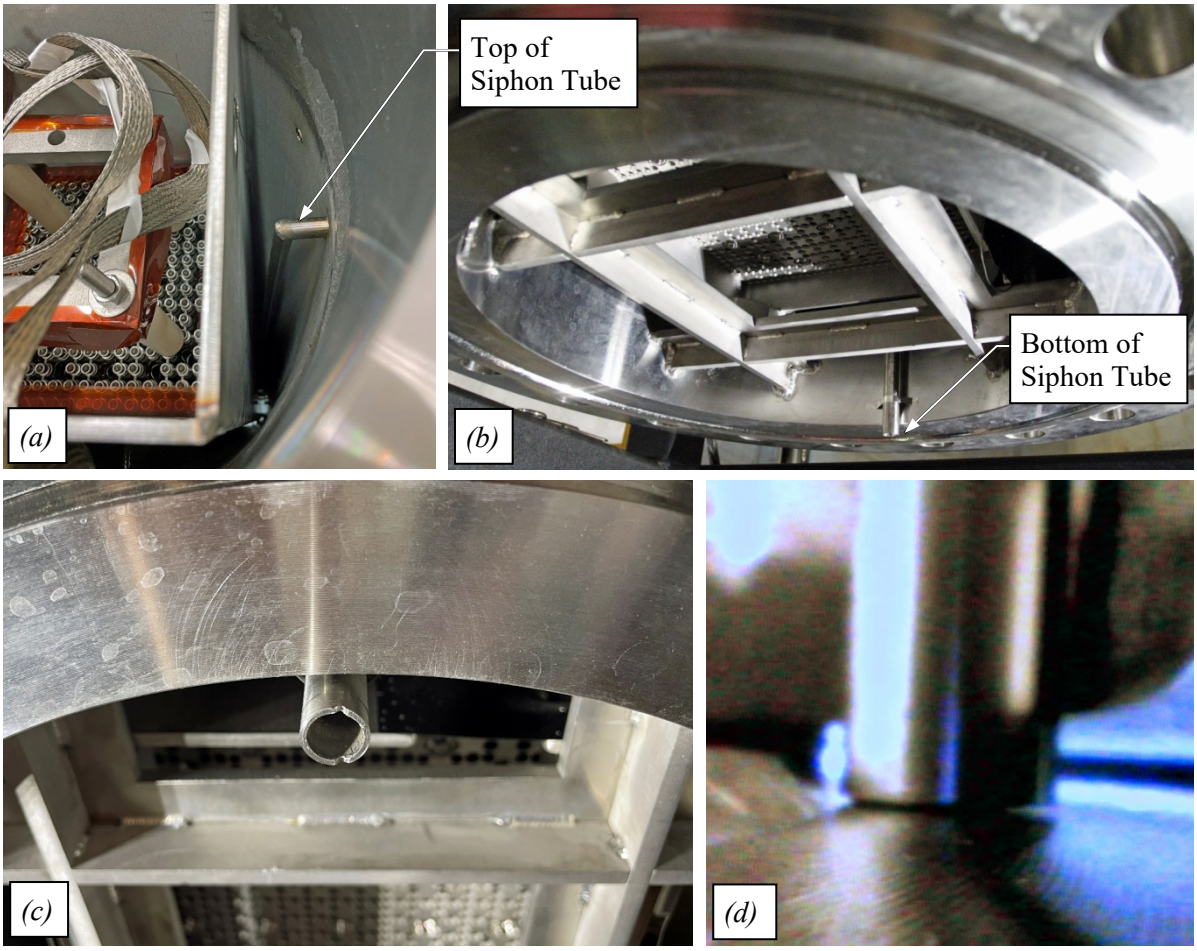

Figure 2-12 *a*) Photo of the top of the siphon tube used for bulk filling and draining of water. *b*) Photo of the bottom of the siphon tube. *c*) Closeup photo of the bottom of the siphon tube after being cut. *d*) Borescopic photo of the siphon tube resting on the bottom flange.

A photo of the complete ADCS pressure vessel is shown in Figure 2-13. The pressure vessel was mounted on a stand comprised of fixture table components and steel framing. This stand elevated the ADCS pressure vessel off the CYBL vessel floor, which allowed viewing access to the sight glass located on the bottom flange.

Figure 2-13 Photo of the ADCS pressure vessel.

A diagram of the test setup including the pressure vessel is shown in Figure 2-14. Bellows-sealed valves form the boundaries to the main internal volume of the PV. The left PV isolation valve leads to the main vacuum pump line (green), consisting of a Leybold EcoDry 40+ scroll pump and a Leybold MAG W 300 iP turbo pump, as well as the mass spectrometer (purple), which uses an Edwards nXDS6i scroll pump and an Edwards nEXT070 turbomolecular pump to maintain a high vacuum within its sample chamber. The right PV isolation valve leads to the branch with the MKS and Setra pressure transducers as well as the helium pressurization line (red), while the center PV isolation valve is used for water filling and draining (blue).

Altogether, the vacuum-tight design minimizes leakage and allows for fine control of both sub-atmospheric pressures and high pressures up to 800 kPa. The pressure vessel maximum allowable working pressure (MAWP) is 2,380 kPa (330 psig) – this value is based on the lowest hydrotest pressure examined for the sight glass. The pressure vessel has been designed to minimize separation between assembly components and instrumentation through the use of blind flanges with penetrations for TCs and instrumentation.

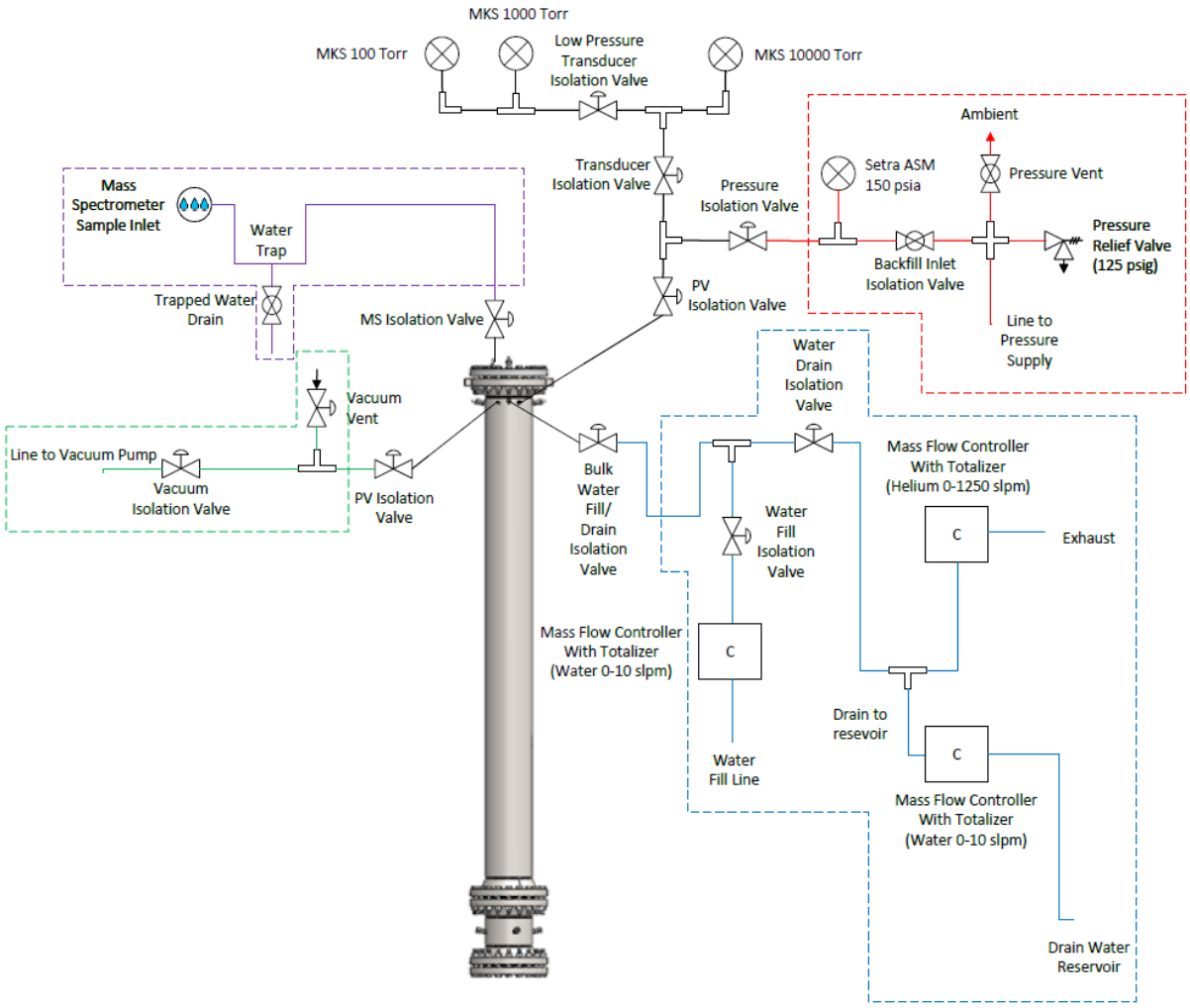

Figure 2-14 Diagram of ADCS pressure/vacuum system.

2.7 Instrumentation

This section will describe the instrumentation used to measure temperature and pressure during this test series, as well as instrumentation specific to moisture/water content measurement.

2.7.1 Thermocouples

Temperatures were measured using type-T thermocouples for the lower pressure vessel region and type-K thermocouples throughout the rest of the ADCS and measuring ambient temperatures using the standard ASTM calibration specifications (ASTM, 2017). No additional calibrations were performed. A coordinate system was defined with an origin ($z = 0$) at the top of the bottom nozzle on the assembly, where the rectilinear z-coordinate runs along the axial length of the pressure vessel towards the upper blind flange (see Figure 2-15). The ambient thermocouples are installed on the interior of the CYBL vessel, along quadrant 3 and 12 inches off the vessel wall – the list of ambient TCs and their axial locations is given in Table A-1. The TCs installed along the surfaces of the heater rods are shown in Table A-2, while the TCs installed on the basket and the interior of the ADCS pressure vessel are shown in Table A-3. The TCs installed on the external surfaces of the pressure vessel and the fittings at the vessel penetrations are listed in Table A-4. As shown in Figure 2-16, the TCs were installed with respect to the heater assembly, which was divided into four quadrants, specified by a quadrant number and a cardinal direction associated with

the CYBL facility. Note that the cardinal directions within the CYBL facility do not coincide with global cardinal directions.

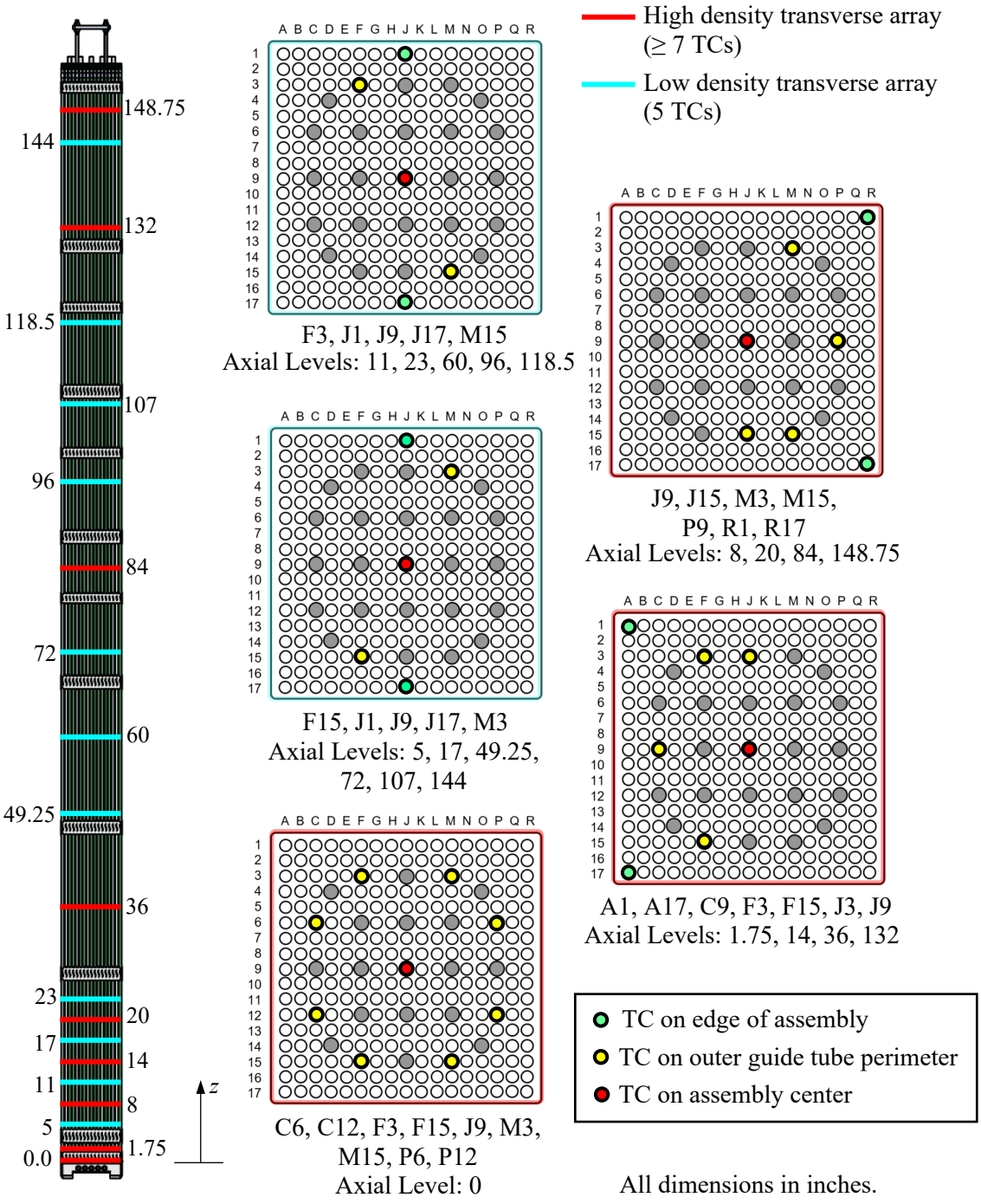

Figure 2-15 Diagram of heater assembly thermocouple locations.

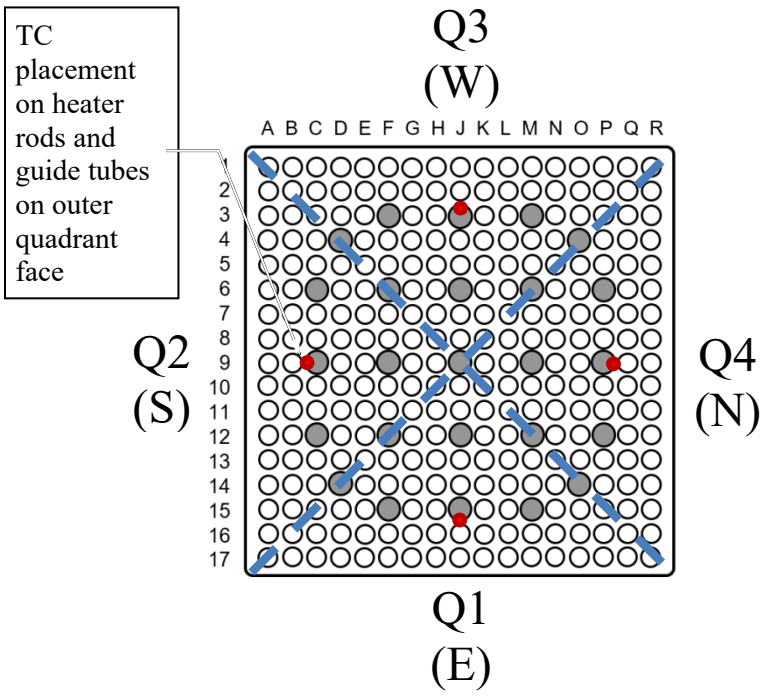

Figure 2-16 Visualization of heater assembly quadrants and thermocouple placement on heater rods.

The type-T TCs are intended to detect the presence of water by measuring sharp temperature changes that would be indicative of phase change during the vacuum drying procedure. The effective measurement range of the type-T TCs installed on the ADCS runs from 0 to 370 °C. Under vacuum, the vapor pressure of the water inside water-retaining cavities will decrease and allow water to evaporate. As the rate of evaporation increases with decreasing pressures, the liquid temperature drops through evaporative cooling. Freezing may also occur if the enthalpy of fusion is exceeded near areas of restricted flow.

The TCs on the basket are shown in Figure 2-17, while the TCs on the ADCS pressure vessel are shown in Figure 2-18. The TCs for the basket and pressure vessel were installed on the exterior surfaces. Most basket TCs on the lower half of the basket have corresponding symmetry TCs on the same axial level in quadrants 180 degrees apart, as indicated by blue dots in Figure 2-17.

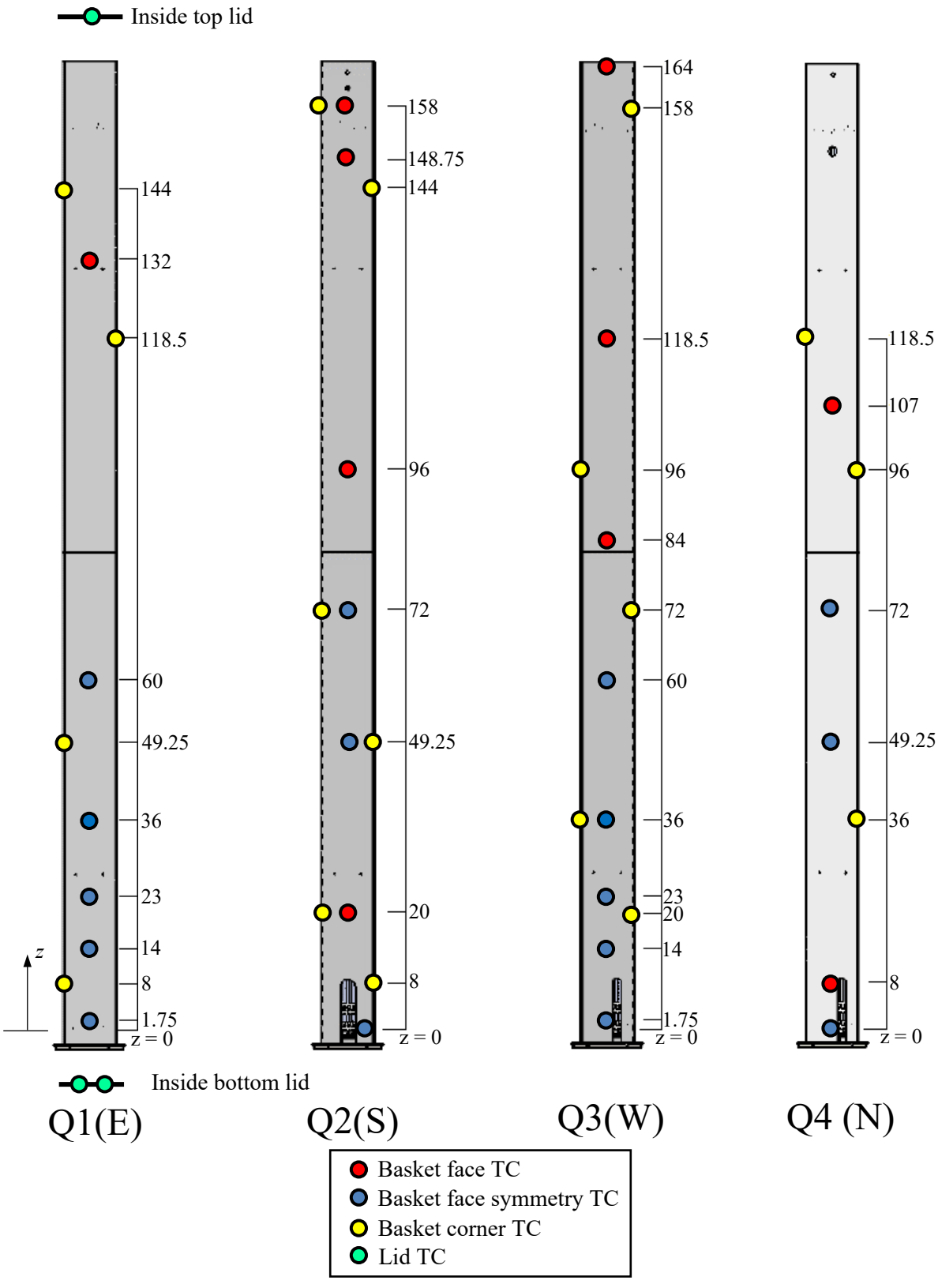

All dimensions in inches.

Figure 2-17 Diagram of basket thermocouple locations.

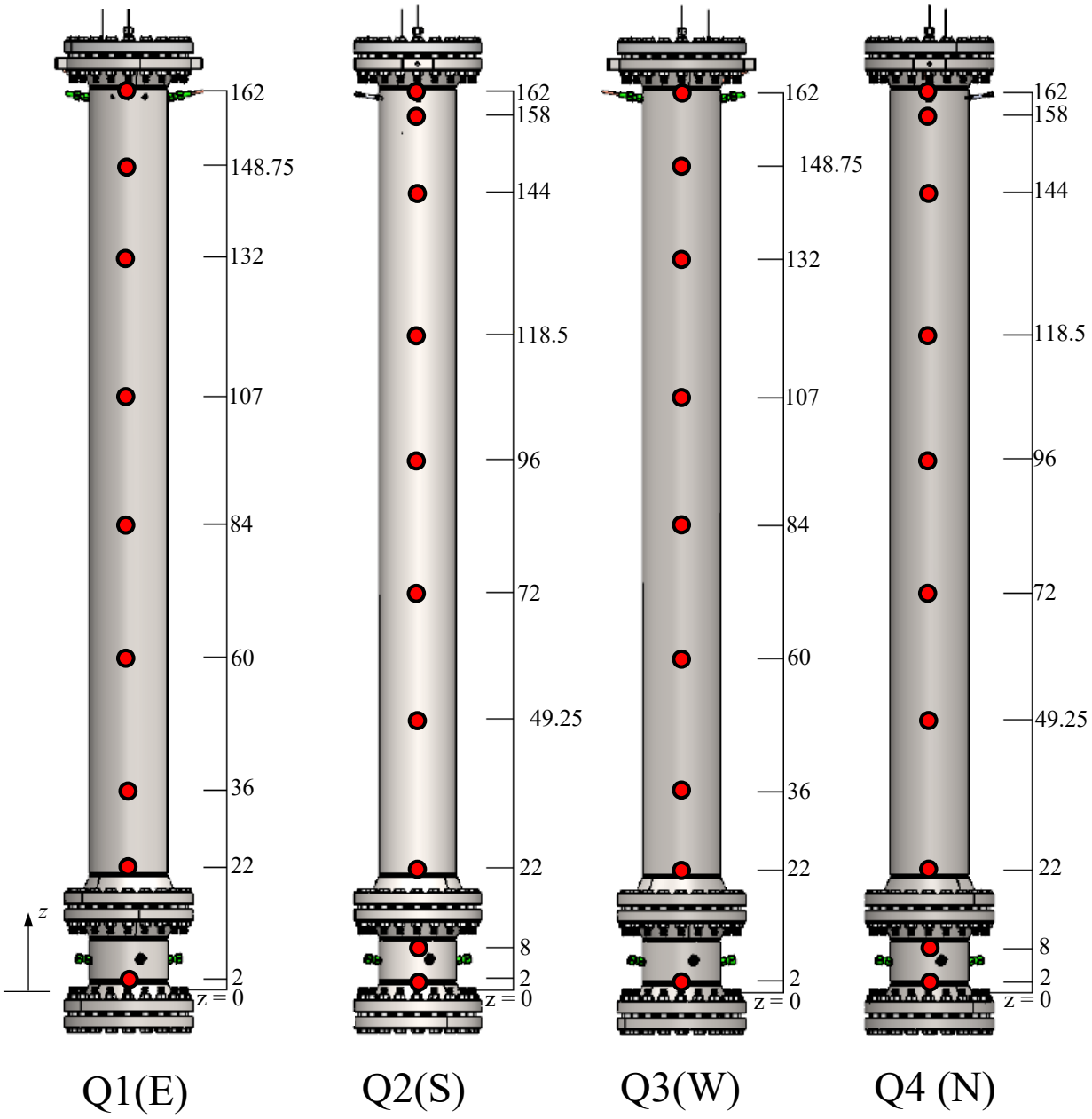

All dimensions in inches.

Figure 2-18 Diagram of ADCS pressure vessel thermocouple locations.

2.7.2 Pressure Measurement and Control

Multiple transducers are employed to provide data for various pressure ranges during the drying test. They are installed external to the PV on VCR fittings and separated with a series of isolation valves until measurement is needed.

An MKS Model 629F heated capacitance manometer rated at 1,333 kPa (10,000 Torr) is employed as an absolute pressure transducer. This manometer is meant to provide overarching pressure measurement for backfill pressurized operations (222 kPa) and vacuum operations (100 mTorr) in the pressure vessel. The

corrosion- and fouling-resistant Inconel sensor measures pressure directly (independent of gas composition) and is maintained at a temperature of 100 °C after a warm-up period of 4 hours, which will ensure that water will not condense within the sensor. The instrument has a resolution of 0.001% full-scale (FS) and accuracy of 0.12% of reading, and it is calibrated with a traceable reference standard. Measurements below 100 Torr were relegated to two additional vacuum transducers for higher accuracy.

Two MKS Baratron D28F heated dual-range capacitance manometers were used as absolute pressure transducers for operations under low vacuum. One of the D28F dual-range manometers is rated for 1,000 Torr with a 100 Torr secondary output, while the other D28F dual-range manometer is rated for 100 Torr with a 10 Torr secondary output; these secondary outputs are read simultaneously with the primary FS outputs. These manometers, like the MKS 629F model, have corrosion- and fouling-resistant Inconel sensors and can measure pressure independent of gas composition. The manometers are also maintained at 100 °C to prevent water condensation. Both D28F manometers have a resolution of 0.001% FS and accuracy of 0.25% of reading, and they are calibrated with a traceable reference standard. This implies a minimum pressure measurement of 0.013 Pa (1 mTorr) for the test series as limited by the 1.33 kPa (100 Torr) dual-range manometer. These instruments are mounted vertically in a shared cross with the D29F MKS transducer that is isolated from the pressure vessel via a bellows-sealed valve.

A Setra Model ASM high-accuracy pressure transducer is used to monitor pressure while backfilling the PV for drainage and blowdown. It has an accuracy of ±0.05% over a 345 kPa (50 psia) FS range, or ±0.10 kPa (±0.025 psia), and was calibrated to a primary standard traceable to NIST. The instrument interfaces with the pressure vessel via a pressure train leading from the top blind flange, which is separated from the manifold holding the main vacuum transducers. This branch includes a pressure relief valve, and it is isolated during vacuum drying tests to reduce leakage.

An Alicat Scientific PC-series single-valve pressure controller was used to set the fill pressure imparted to the pressure vessel from the helium cylinder. This controller has a NIST-traceable calibration to ±0.125% accuracy and ranges up to 1,034 kPa (150 psia) FS, with an operating range down to 0.5% FS. Repeatability of setpoint is specified at ±0.08% FS.

An Alicat Scientific LCR-series liquid flow controller was used to fill the ADCS with deionized water. Its maximum flow capacity is 0.12 kg/s (10 slpm), and the controller has a NIST-traceable calibration to ±2% FS accuracy.

2.7.3 Water Content Measurement

Mass spectroscopy is a nontraditional method for measuring the relative moisture concentration in gas (i.e., parts per million by volume, ppm_v). In mass spectroscopy, a small sample stream (1 to 20 scm^3/min, where scm^3 is a cubic centimeter of gas referenced at a standard temperature and pressure, depending on sample pressure) is ionized and drawn into a vacuum chamber through a quadrupole filter that influences how ionized species interact with the ion detector. Because mass spectroscopy draws a small sample flow, perturbations of the system pressure may be expected. Furthermore, adsorption and desorption of water on the small-bore stainless steel or glass capillary sample tubes can be an issue, especially as the sample flow rate drops with falling sample pressure. Heating the sample lines and quadrupole minimizes the problem, but it will still take several minutes of sample flow for equilibrium to be reached. For slowly changing transient operations expected in drying operation, the anticipated lags are expected to be manageable. With a properly designed inlet, the high temperature and the wide range of pressures inside the pressure vessel can be accommodated.

The MS uses a scroll pump in combination with a turbo molecular pump to evacuate the internal volume and reduce the pressure within the spectrometer. This allows sample gases to flow into an ion source, which ionizes the molecular components of the sample gas. The ionized molecules are guided by a potential gradient between the ion source and ground to a quadrupole, which filters the molecules based on their mass-to-charge ratio m/z (amu/Coulomb). The quadrupole influences how the charged molecules

impact the MS detector – either a secondary electron multiplier (SEM) or a Faraday cup – the mass spectrometer outputs the number of counts of ion-detector collisions based on *m*/*z*. The relative concentrations of each molecular component can thus be calculated from the ion detector collision count peaks at each *m*/*z* value.

A given gas sample will have multiple peaks based on how the molecules are ionized (singly or doubly charged) and the presence of molecular isotopes. For each molecule, determining a relative concentration amounts to accounting for the major peak of that molecule, which is associated with the molecule's most common ionic species. For example, as shown in Figure 2-19, the three peaks associated with nitrogen come from singly-charged $^{28}N_2$ (28 amu/1 C = 28 amu/C), doubly-charged $^{28}N_2$ (28 amu/2 C = 14 amu/C), and singly-charged $^{29}N_2$ (29 amu/1 C = 29 amu/C). The 28 amu/C peak is the largest peak in the mass spectrum of nitrogen, so it is the peak used for quantification. A method could have been developed using all three peaks, but the analysis would take longer to complete. Since the drying process is transient, a rapid method was needed to resolve temporal changes and only the major peaks for water, helium, nitrogen, oxygen, and argon were analyzed. The resulting analysis time for the method developed was about 45 seconds.

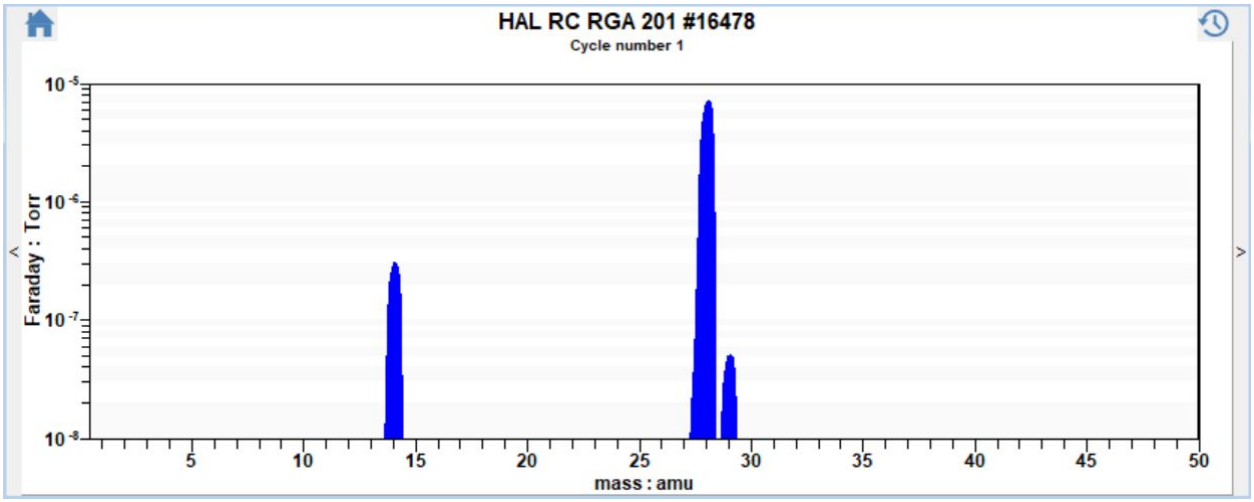

Figure 2-19 Mass spectrum of air showing the major peaks for nitrogen.

The amount of residual water (18 amu) detected will help define the effectiveness of the drying procedures implemented. An advantage of using an MS is that all other gaseous species are analyzed. For vacuum drying, the amount of air components can be used to evaluate the air leakage into the system. If used to monitor a commercial dry cask, an MS can also detect hydrogen generation that would indicate radiolysis or noble gas fission products (e.g., Kr-85 or Xe-137) that would indicate a leaking fuel rod.

Two Hiden Analytical mass spectrometers will be used to measure water content in the ADCS. The HPR-20, shown in Figure 2-20, is a 6 mm quadrupole mass spectrometer with both secondary electron multiplier (SEM) and Faraday cup detection capabilities. These detectors can be employed to analyze transient gas concentrations in gas samples from the pressure vessel. The samples are obtained via stainless-steel capillary tubes, whose inner diameter changes depending on the sampling pressure ranges. The HPR-20 MS was upgraded in FY22 to include two sample ranges – 10 to 100 kPa (76 to 760 Torr) and 85 to 850 kPa (638 to 6,380 Torr). Pressurized nitrogen can be used to dry out both HPR-20 sampling lines, and the nitrogen can be flushed out with helium to establish a helium background for water content measurements.

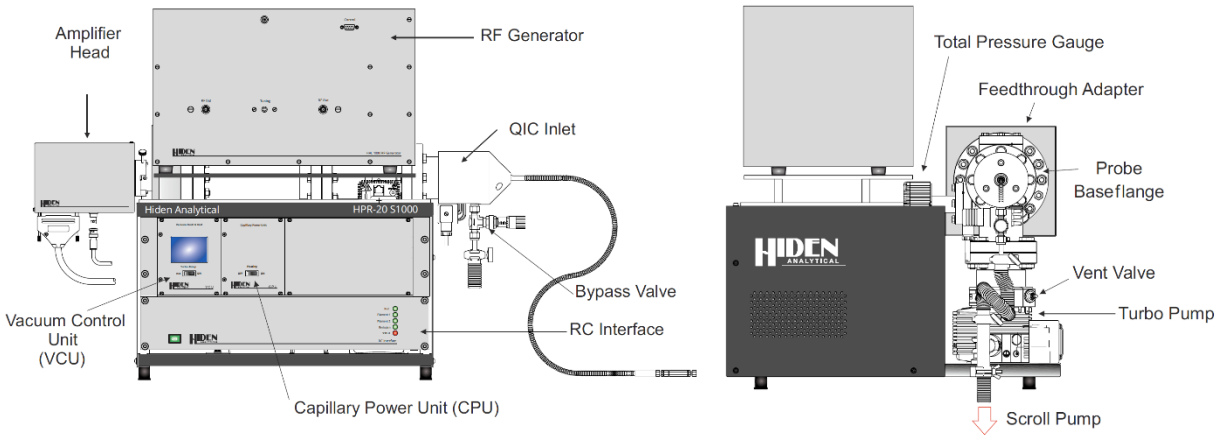

Figure 2-20 Hiden Analytical HPR-20 mass spectrometer system with a QIC dual-stage sampling head for measuring water content (Hiden Analytical Limited, 2018a).

The HPR-30, shown in Figure 2-21, is a 6 mm quadrupole mass spectrometer with a Faraday cup detector employed to analyze transient gas concentrations in gas samples from the pressure vessel obtained via stainless-steel capillary tubes with varying inner diameters to cover three vacuum ranges. This HPR-30 MS was used in previous testing (Salazar *et al.*, 2020), but the system was modified to allow for sampling between 0.05 to 0.5 kPa (0.4 to 4 Torr), 0.4 to 4 kPa (3 to 30 Torr), and 4 to 40 kPa (30 to 300 Torr). The low-vacuum range of 4 to 40 kPa can be used for drying out the mass spectrometer with nitrogen and establishing a helium sampling background.

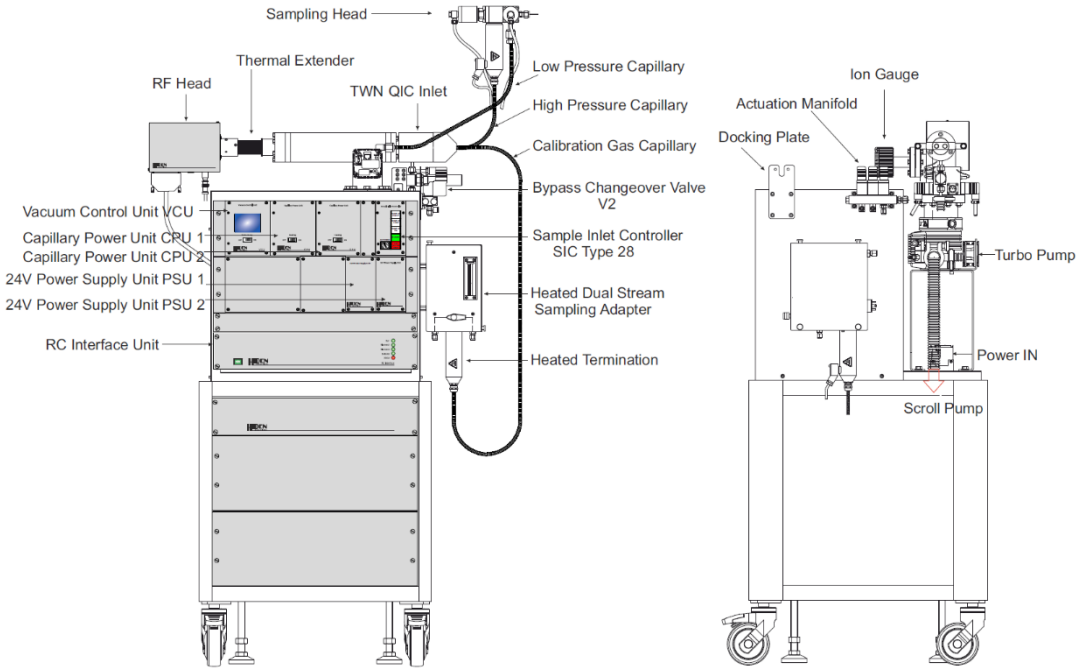

Figure 2-21 Hiden Analytical HPR-30 mass spectrometer system with a QIC dual-stage sampling head for measuring water content (Hiden Analytical Limited, 2018b).

All of the new HPR-30 vacuum ranges can be used for vacuum drying tests, and the 4 to 40 kPa sampling range on the HPR-30 overlaps with the 10 to 100 kPa sampling range on the HPR-20. Therefore, the two mass spectrometers cover a continuous sampling range from 0.05 to 850 kPa (4 to 6,380 Torr) – see Figure 2-22.

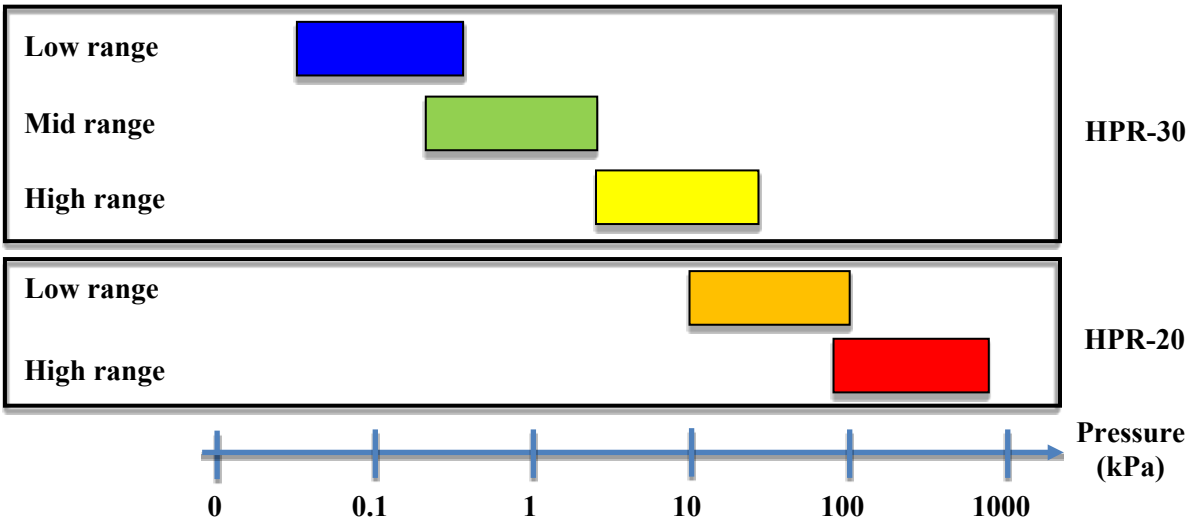

Figure 2-22 HPR-20 and HPR-30 sampling pressure ranges.

For FY22, the upgraded HPR-20 MS was calibrated to detect water content using a Michell DG2 two-stage dew point (DP) generator (-40 °C to +20 °C dew points). This was the first time the HPR-20 MS was used for water content measurements, as previous testing (Salazar *et al*., 2020; Durbin *et al*., 2021; Pulido *et al*., 2022) utilized the HPR-30 MS prior to the FY22 upgrades. The Michell DG2 DP generator uses a dry gas source such as ultra-high purity helium or air and generates a split stream that is mixed with moisture at a controlled temperature to generate a gas with a known dew point between -40 °C to +20 °C. The dew point of the calibration gas was verified by passing through a Michell S8000 chilled mirror hygrometer that can provide precision measurements to -65 °C dew point. The MS was calibrated for moisture concentrations between zero and 31,000 ppm_v using helium as the background gas. The calibration procedure was used to generate a relative sensitivity factor for water that is used to calibrate the mass spectrometer water content measurements to the chilled mirror hygrometer measurements. This calibration procedure is described in great detail in the FY20 waterproof heater rod testing report (Salazar *et al.*, 2020).

The result of the calibration conducted for this test series is shown in the linear regression of the raw data in Figure 2-23. The relative sensitivity factor was calculated to be 4.061, taken from the slope of the linear regression of the raw data. The intercept was previously defined as the detection limit of the mass spectrometer. This intercept was calculated to be 1,519 ppm_v. The linear regression had a coefficient of determination of $R^2 = 0.9991$ and a standard error of 921.7 ppm_v. The 95% confidence interval for the regression, based on the *t*-statistic of 1.975 and the standard error, or SE, was ±1,820 ppm_v.

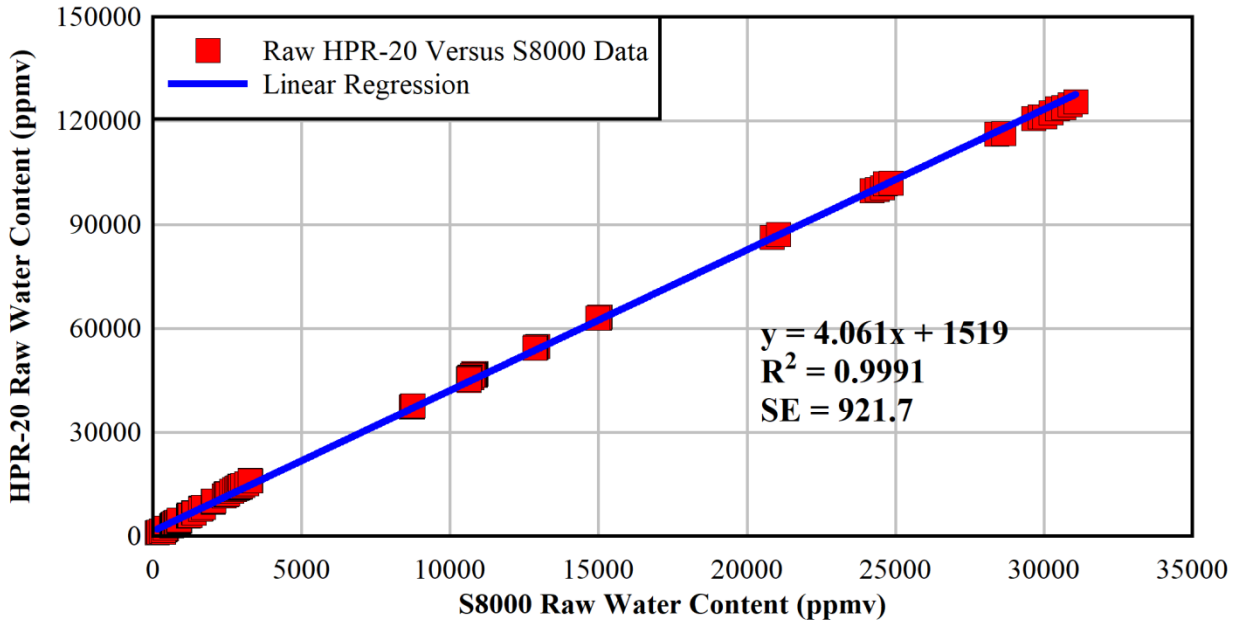

Figure 2-23 Linear regression of the raw water content measurements for determining the relative sensitivity factor for water in a helium background when calibrating the HPR-20 mass spectrometer with respect to the S8000 chilled mirror hygrometer.

2.8 Power Control

The electrical power supplied to the heater rods within the ADCS pressure vessel was controlled using a digital silicon-controlled rectifier (SCR). The SCR was used to maintain the desired temperatures in the ADCS and to have them remain within safe operating margins. The device software provided digital power setpoints to the SCR that was controlled using a PXIe DAQ and based on external power feedback from a calibrated diagnostic unit (APlus) installed on the 120 VAC power supply. Diagnostic measurements from the APlus were available from the SCR by connecting the power lines to the available ports.

Figure 2-24 shows the power control setup, and Table 2-1 lists the instruments used for power control and measurement. The full-scale settings for SCR control were defined as 1,000 W, 120 V, and 8.333 A. The SCR shared the same ground as the power source.

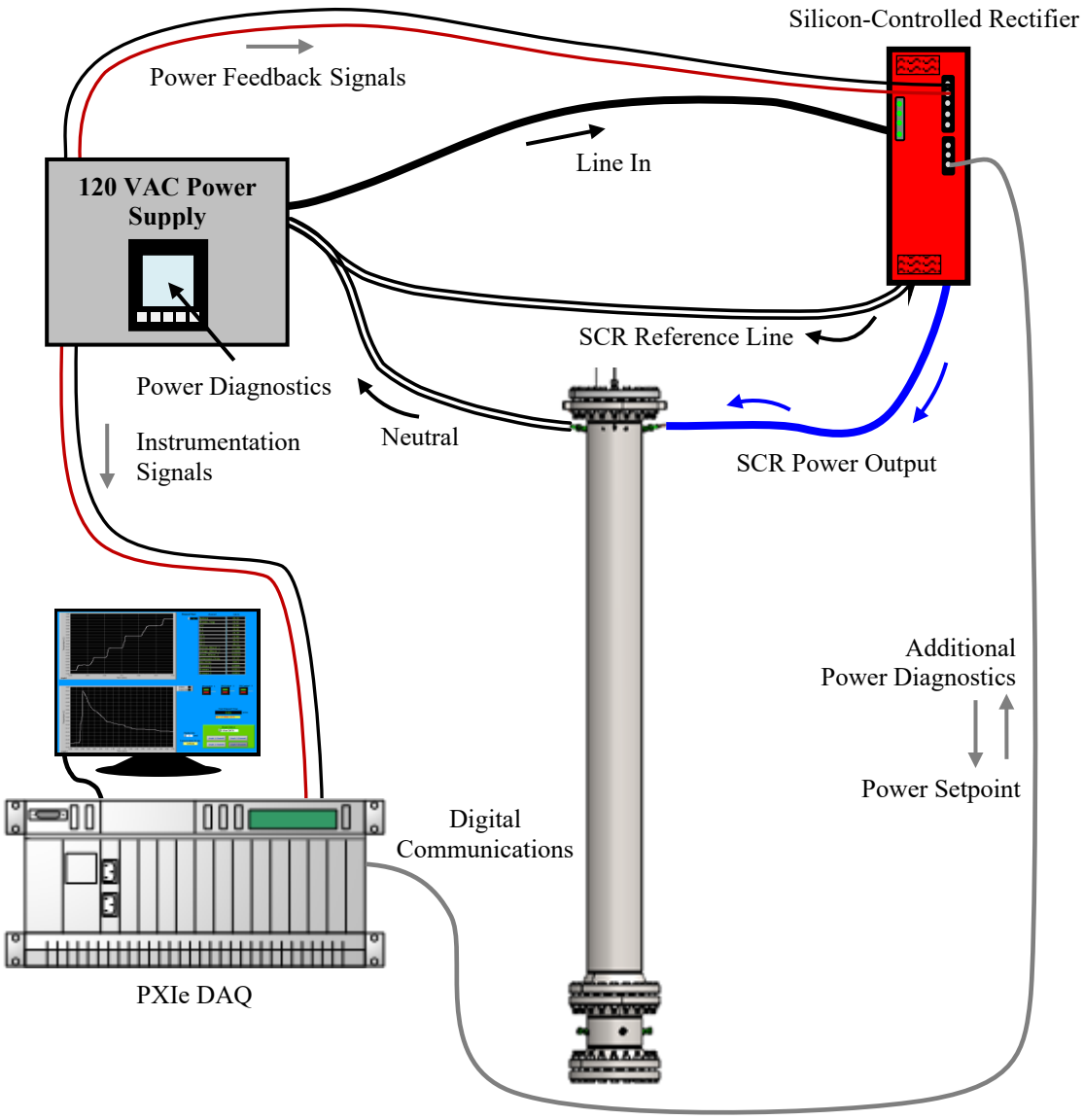

Figure 2-24 Diagram of the power control setup for the ADCS.

Table 2-1 List of power control equipment.

Description	Manufacturer	Model
Digital SCR AC Power Controller	Control Concepts	uF1HXLGI-130-P1RSZ
Power Monitor with System Analysis	Camille Bauer	APlus
Data Acquisition System (DAQ)	National Instruments	PXIe

Figure 2-25 shows how electrical and neutral connections to the ADCS were made. The “hot” electrical connection to an exterior power supply was established via the installation of a primary bus plate in contact with the heater rods and a secondary bus plate in contact with the primary bus plate via Monel rods (Figure 2-25a). The four Monel rods are threaded into four of the heater rods, and the Monel rods are connected to the secondary bus plate using nuts and washers to establish electrical connectivity throughout the heater rods and the two bus plates. In this way, a uniform power can be supplied to all

heater rods – details on the power supply are given in Section 2.8. Neutral straps connecting to an electrically neutral wire were wrapped around the top-most grid spacer and fixed in place using shim stock spot welded onto the grid spacer (Figure 2-25b). A separate, shorter neutral strap was fixed to both the bottom nozzle and the lower pressure vessel (Figure 2-25c).

Figure 2-26 shows where the "hot" and neutral electrical connections are made and how insulation was installed to prevent shorting between the heater assembly and the conductive components interior to the pressure vessel, such as the basket. Kapton insulation was wrapped around the top of the heater rods and the primary bus plate (Figure 2-26a). The Kapton insulation was also wrapped around the secondary bus plate and placed between the nuts and washers (Figure 2-26b). Hollow ceramic rods were placed around the Monel rods for additional electrical insulation (Figure 2-26b). The neutral strap was fed through the basket to access the exterior of the ADCS vessel – an example of this during preliminary electrical testing is shown in Figure 2-26c.

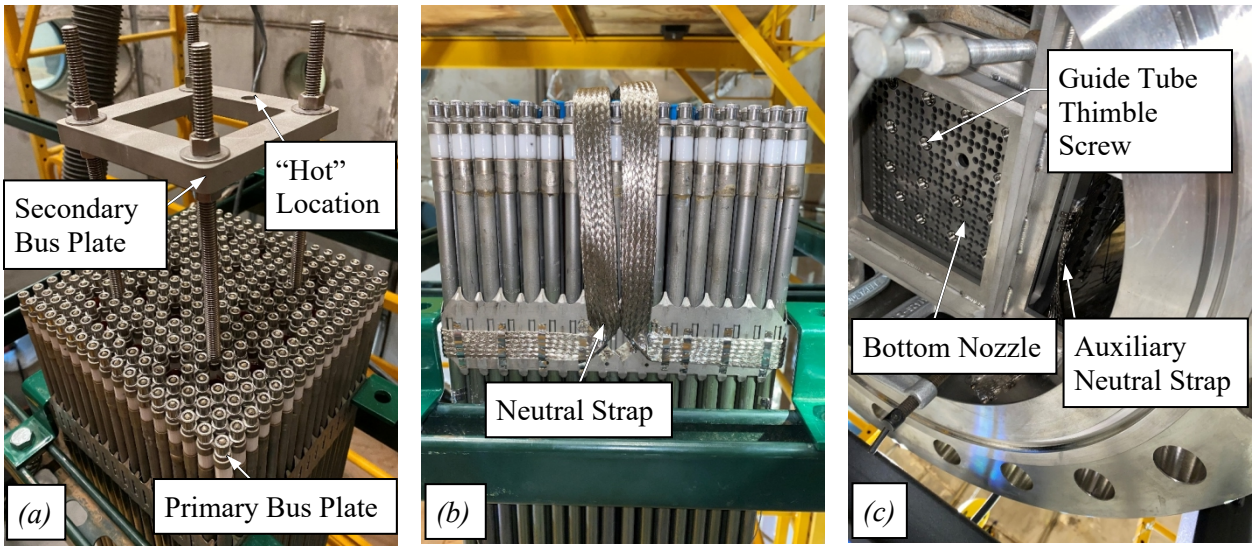

Figure 2-25 ***a*) Primary and secondary bus plates for "hot" electrical connection used to supply power to heater rods. *b*) Neutral strap on top-most grid spacer. *c*) Separate neutral strap on bottom nozzle and lower pressure vessel.**

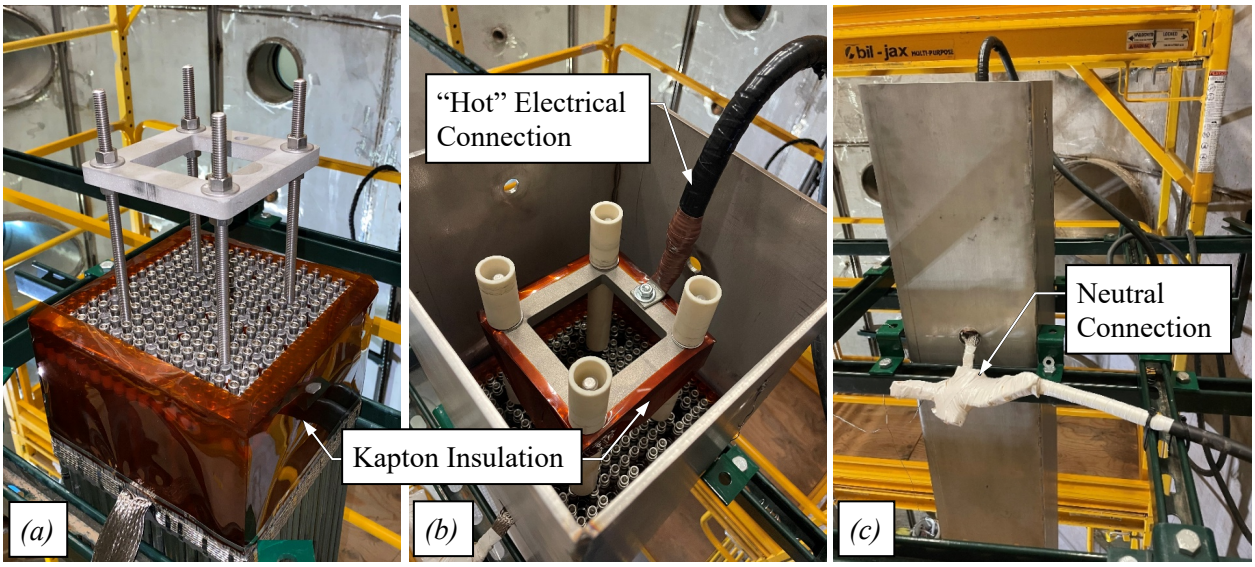

Figure 2-26 *a*) Kapton insulation to prevent shorting between heater rods and basket. *b*) "Hot" electrical connection and Kapton insulation on Monel rod washers. *c*) Neutral electrical connection from heater assembly through the basket. Note that electrical connections shown here are for testing purposes.

The ADCS was built to scale up from earlier testing efforts from the Dashpot Drying Apparatus, which was built to investigate the response of the dashpot region of a simulated PWR fuel assembly to commercial drying cycles (Pulido *et al.*, 2022). The DDA test procedures were set up to simulate the drying procedures performed on the High-Burnup Demonstration Project cask as closely as possible. ADCS testing will apply lessons learned from DDA testing to a prototypic-length scale simulated PWR assembly.

This page is intentionally left blank.

3 CURRENT ADCS STATUS

3.1 Final Construction

Final construction of the ADCS was started in late August 2022. The final electrical connections, including the "hot" and neutral pressure fittings as well as insulation to prevent shorting, are shown in Figure 3-1. The top flange was the final component of the pressure vessel and was installed on September 9, 2022, as depicted in Figure 3-2.

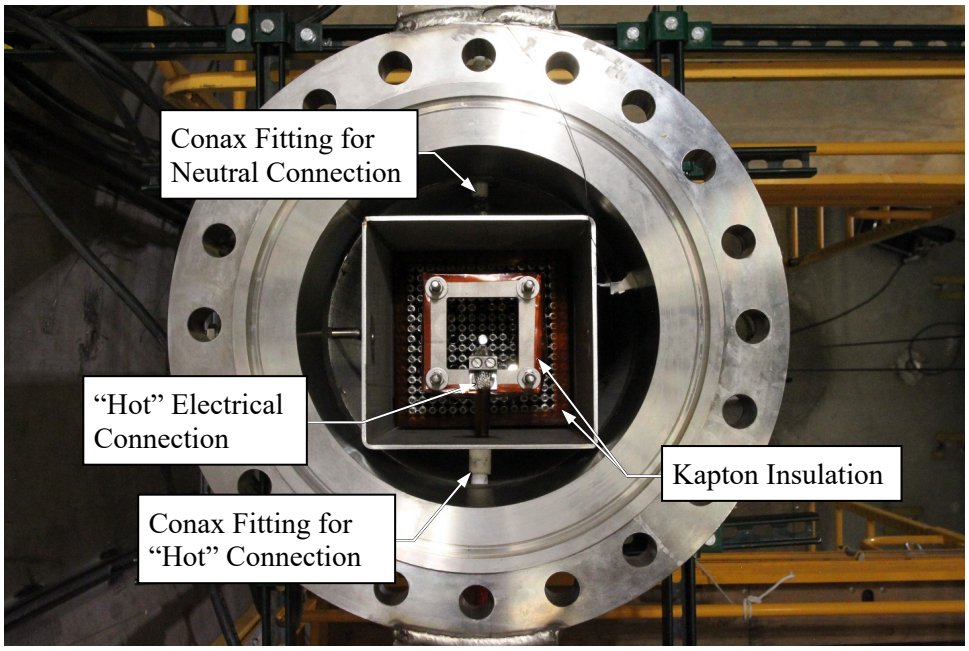

Figure 3-1 Final ADCS electrical configuration. The top flange is not installed in this image.

Figure 3-2 Installation of top flange.

3.2 Power Functionality Testing

In preparation for ADCS testing, power was supplied to the fully assembled apparatus. The thermal response of the center of the fuel assembly is reported in Figure 3-3 for a test started on September 15, 2022, with an applied power of 2.0 kW. The M15 thermocouple is reported at the z = 118.5 in. level due to a possible failure of the J9 TC at that level. This functional test was conducted with an internal absolute pressure of 200 kPa of helium.

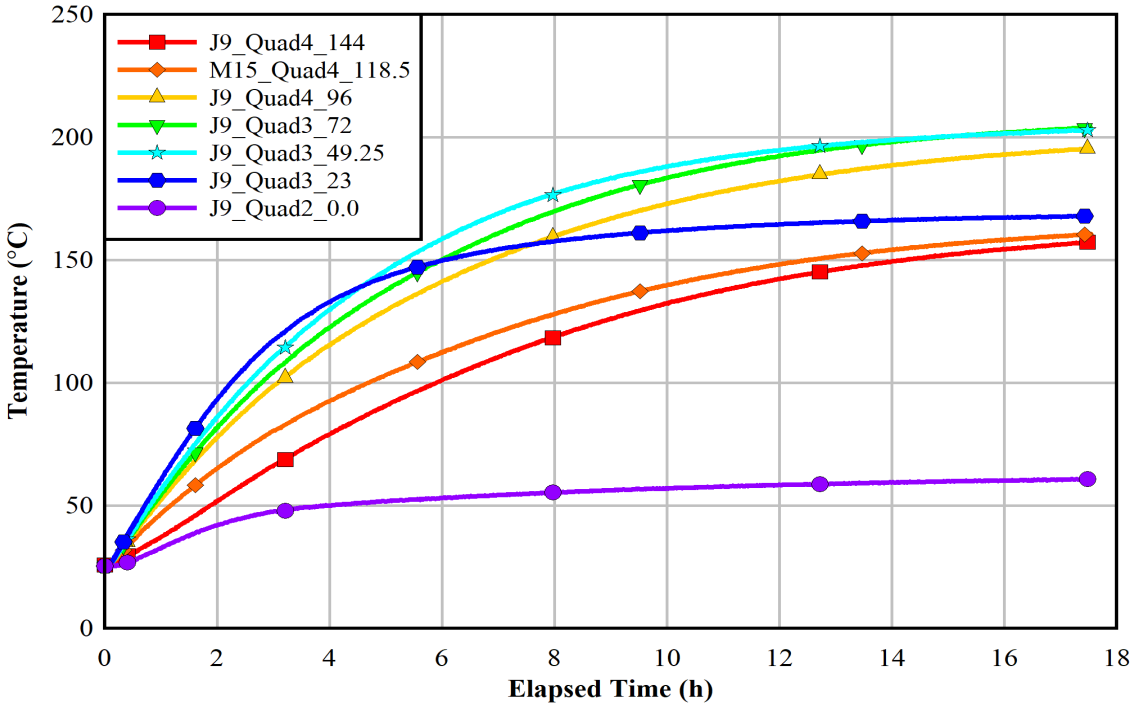

Figure 3-3 Thermal response throughout the center of the ADCS fuel assembly at an applied power of 2.0 kW.

Figure 3-4 shows the power (left), voltage (right), and current (right) for the operational test conducted on September 15, 2022. The average and standard deviation of the power over the duration of the test were 2,004 and 8 W, respectively. Additional improvements to the power control system are planned, which should improve both setpoint and observed fluctuations. Figure 3-5 shows a histogram of the measured power and the equivalent normal distribution. For reasons that are currently not understood, the applied power appears to be bimodal. This behavior could be due to an underdamped control algorithm. This distribution will be evaluated again once the final power control system has been implemented.

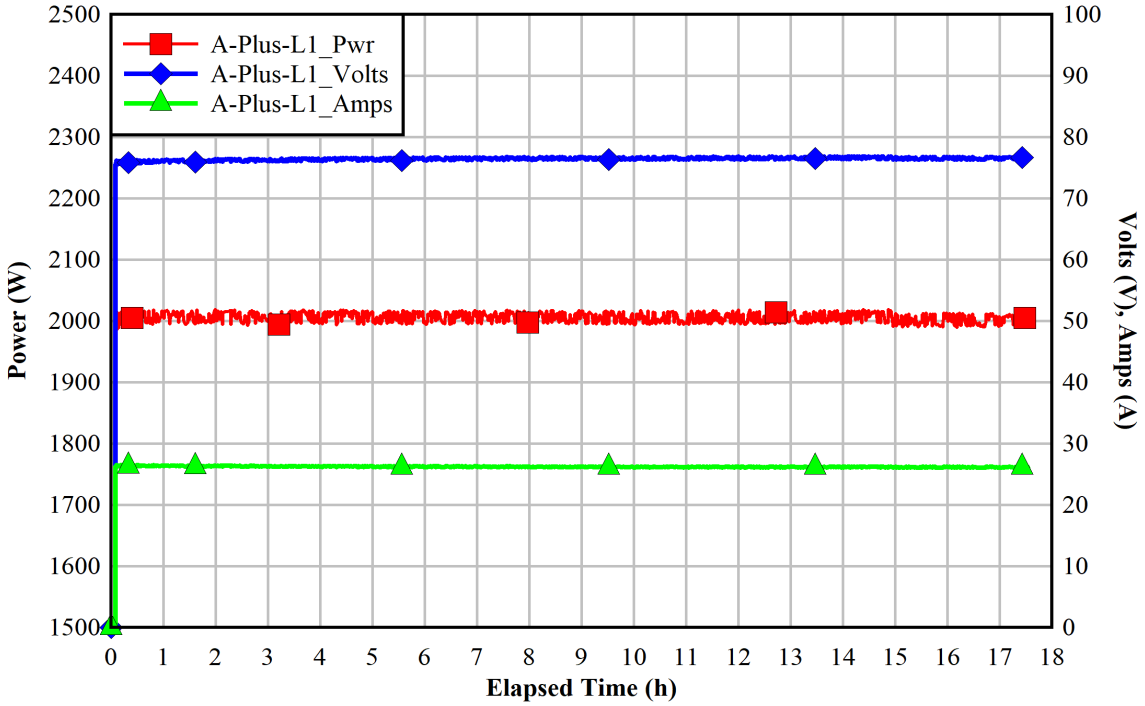

Figure 3-4 Demonstration of power control at 2.0 kW.

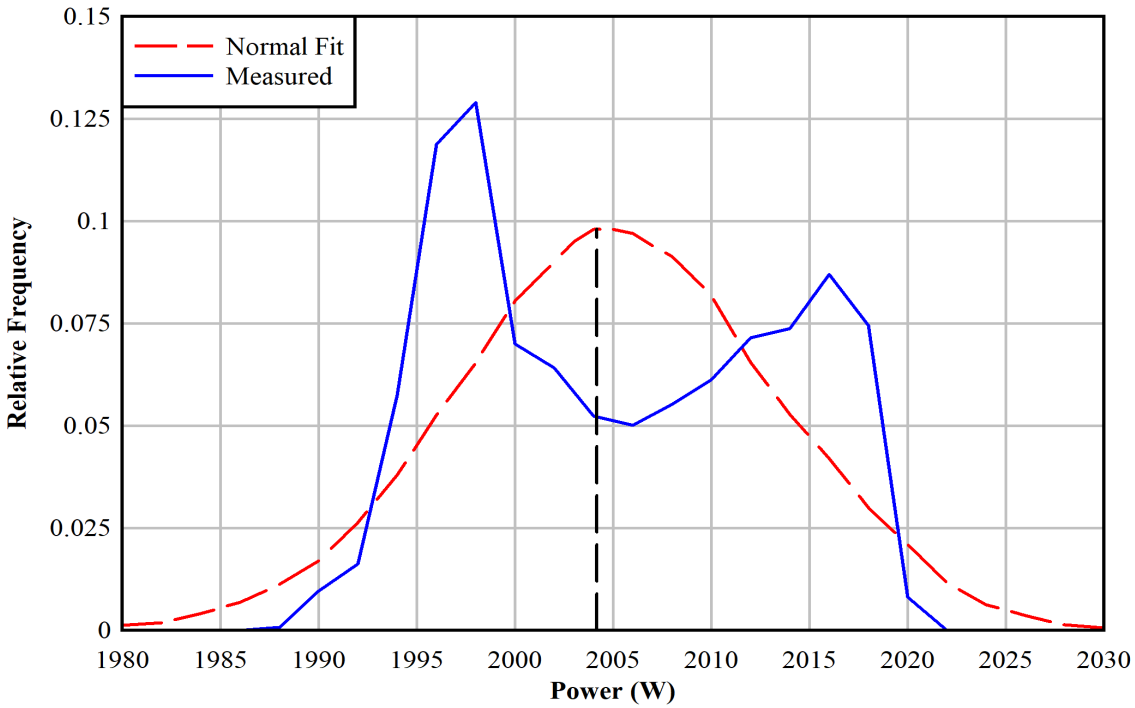

Figure 3-5 Histogram of power for a nominal setting of 2.0 kW.

3.3 Future Work

Construction and instrumentation of the Advanced Drying Cycle Simulator vessel was finalized at the end of FY22. Preliminary functionality testing of the power control and thermocouples has been completed. A limited number of internal thermocouples have been identified as nonfunctioning and repair will be attempted. Also, a refined power control will be implemented. Pressure and vacuum leak testing will also be a priority in the near term.

Plumbing for the bulk water system including fill and drain tanks are expected to be completed in the first quarter of FY23. Additional plumbing for the mass spectrometers will also be completed in this time frame. All inflows and discharges into or from the vessel will be recorded by mass flow meters or controllers.

At the conclusion of system operational tests, integrated testing will focus on reproducing the conditions measured in the High Burnup Demonstration Project (EPRI, 2019). The performance of the ADCS assembly measured during the September 15, 2022 operational test indicates that the assembly has significant margin to replicate the High Burnup Demonstration heat-up and vacuum drying cycle. The installed instrumentation will provide an unprecedented level of understanding of commercial drying cycles at both quasi-steady state hold points and during transients.

4 REFERENCES

ASTM International (2016). Standard Guide for Drying Behavior of Spent Nuclear Fuel (C1553-16). ASTM Book of Standards Volume 12.01. West Conshohocken, PA.

ASTM International (2017). Standard Specification for Temperature-Electromotive Force (emf) Tables for Standardized Thermocouples (E230/E230M-17). ASTM Book of Standards Volume 14.03. West Conshohocken, PA.

Bryan, C. R., Jarek, R. L., Flores, C., & Leonard, E. (2019). Analysis of Gas Samples Taken from the High Burnup Demonstration Cask (SAND2019-2281). Sandia National Laboratories. Albuquerque, NM.

Colburn, H. A. (2022). Small Scale Drying: FY22 Interim Report. PNNL-33178. Pacific Northwest National Laboratory, Richland, WA.

Durbin, S. G., E. R. Lindgren, R. J. M. Pulido, A. Salazar III, and R. E. Fasano (2021). Update on the Simulation of Commercial Drying of Spent Nuclear Fuel (SAND2021-11828 R). Sandia National Laboratories. Albuquerque, NM.

EPRI. High Burnup Dry Storage Research Project Cask Loading and Initial Results (2019). Technical Report 3002015076. Palo Alto, CA.

Fort, J. A., Richmond, D. J., Jensen, B. J., & Suffield, S. R. (2019). High-Burnup Demonstration: Thermal Modeling of TN-32B Vacuum Drying and ISFSI Transients (PNNL-29058). Pacific Northwest National Laboratories. Richland, WA.

Hanson, B. D., & Alsaed, H. A. (2019). Gap Analysis to Support Extended Storage and Transportation of Spent Nuclear Fuel: Five-Year Delta (SFWD-SFWST-2017-000005, Rev 1; PNNL-28711). Pacific Northwest National Laboratory. Richland, WA.

Hiden Analytical Limited (2018a). HPR-20 S1000 User Manual (HA-085-189A). Warrington, United Kingdom.

Hiden Analytical Limited (2018b). TWN QIC Dual Stage Sampling Head Manual (HA-085-850). Warrington, United Kingdom.

Knight, T. W. (2019). Experimental Determination and Modeling of Used Fuel Drying by Vacuum and Gas Circulation for Dry Cask Storage (NEUP 14-7730). University of South Carolina. Columbia, SC.

Knoll, R., & Gilbert, E. (1987). Evaluation of Cover Gas Impurities and their Effects on the Dry Storage of LWR (Light-Water Reactor) Spent Fuel (PNL-6365). Pacific Northwest National Laboratory. Richland, WA.

Nuclear Regulatory Commission (2002). Westinghouse Technology Manual (ML023040131). Washington, D.C.

Nuclear Regulatory Commission (2020). Standard Review Plan for Spent Fuel Dry Storage Systems and Facilities, Final Report (NUREG-2215). Washington, D.C.

Pulido, R. J. M., A. Taconi, A. Salazar, R. E. Fasano, R. W. Williams, B. Baigas, and S. G. Durbin (2022). Response of a Pressurized Water Reactor Dashpot to Commercial Drying Cycles (SAND2022-3813 R). Sandia National Laboratories. Albuquerque, NM.

Salazar, A., Pulido, R. J. M., Lindgren, E. R., & Durbin, S. G. (2019). Advanced Concepts for Dry Storage Cask Thermal-Hydraulic Testing (SAND2019-11281 R). Sandia National Laboratories. Albuquerque, NM.

Salazar, A., Lindgren, E. R., Fasano, R. E., Pulido, R. J. M., & Durbin, S. G. (2020). Development of Mockups and Instrumentation for Spent Fuel Drying Tests (SAND2020-5341 R). Sandia National Laboratories, Albuquerque, NM.

This page is intentionally left blank.

APPENDIX A LIST OF THERMOCOUPLES

Table A-1 List of ambient thermocouples.

#	Type	*z* Position (in.)	Quadrant	DAQ Label
1	T	-24	3	Ambient_Quad3_ -24"
2	T	-12	3	Ambient_Quad3_ -12"
3	T	0	3	Ambient_Quad3_0"
4	T	20	3	Ambient_Quad3_20"
5	T	49	3	Ambient_Quad3_49"
6	T	72	3	Ambient_Quad3_72"
7	T	96	3	Ambient_Quad3_96"
8	T	119	3	Ambient_Quad3_119"
9	T	144	3	Ambient_Quad3_144"
10	T	158	3	Ambient_Quad3_158"
11	T	170	3	Ambient_Quad3_170"
12	T	182	3	Ambient_Quad3_182"

Table A-2 List of heater assembly thermocouples.

#	Type	Coordinate	*z* Position (in.)	Quadrant	DAQ Label
13	T	A1	1.75	2	A1_Quad2_1.75"
14	T	A1	14	2	A1_Quad2_14"
15	K	A1	36	3	A1_Quad3_36"
16	K	A1	132	4	A1_Quad4_132"
17	T	A17	1.75	2	A17_Quad2_1.75"
18	T	A17	14	2	A17_Quad2_14"
19	K	A17	36	3	A17_Quad3_36"
20	K	A17	132	4	A17_Quad4_132"
21	T	C6	0.0	2	C6_Quad2_0.0"
22	T	C9	1.75	2	C9_Quad2_1.75"
23	T	C9	14	2	C9_Quad2_14"
24	K	C9	36	3	C9_Quad3_36"
25	K	C9	132	4	C9_Quad4_132"
26	T	C12	0.0	2	C12_Quad2_0.0"
27	T	F3	0.0	2	F3_Quad2_0.0"
28	T	F3	1.75	2	F3_Quad2_1.75"
29	T	F3	11	2	F3_Quad2_11"
30	T	F3	14	2	F3_Quad2_14"
31	T	F3	23	3	F3_Quad3_23"
32	K	F3	36	3	F3_Quad3_36"
33	K	F3	60	3	F3_Quad3_60"

34	K	F3	96	4	F3_Quad4_96"
35	K	F3	118.5	4	F3_Quad4_118.5"
36	K	F3	132	4	F3_Quad4_132"
37	T	F15	0.0	2	F15_Quad2_0.0"
38	T	F15	1.75	2	F15_Quad2_1.75"
39	T	F15	5	2	F15_Quad2_5"
40	T	F15	14	2	F15_Quad2_14"
41	T	F15	17	3	F15_Quad3_17"
42	K	F15	36	3	F15_Quad3_36"
43	K	F15	49.25	3	F15_Quad3_49.25"
44	K	F15	72	3	F15_Quad3_72"
45	K	F15	107	4	F15_Quad4_107"
46	K	F15	132	4	F15_Quad4_132"
47	K	F15	144	4	F15_Quad4_144"
48	T	J1	5	2	J1_Quad2_5"
49	T	J1	11	2	J1_Quad2_11"
50	T	J1	17	3	J1_Quad3_17"
51	T	J1	23	3	J1_Quad3_23"
52	K	J1	49.25	3	J1_Quad3_49.25"
53	K	J1	60	3	J1_Quad3_60"
54	K	J1	72	3	J1_Quad3_72"
55	K	J1	96	4	J1_Quad4_96"
56	K	J1	107	4	J1_Quad4_107"
57	K	J1	118.5	4	J1_Quad4_118.5"
58	K	J1	144	4	J1_Quad4_144"
59	T	J3	1.75	2	J3_Quad2_1.75"
60	T	J3	14	2	J3_Quad2_14"
61	K	J3	36	3	J3_Quad3_36"
62	K	J3	132	4	J3_Quad4_132"
63	T	J9	0.0	2	J9_Quad2_0.0"
64	T	J9	1.75	2	J9_Quad2_1.75"
65	T	J9	5	2	J9_Quad2_5"
66	T	J9	11	2	J9_Quad2_11"
67	T	J9	14	2	J9_Quad2_14"
68	T	J9	8	2	J9_Quad2_8"
69	T	J9	17	3	J9_Quad3_17"
70	T	J9	20	3	J9_Quad3_20"
71	T	J9	23	3	J9_Quad3_23"
72	K	J9	36	3	J9_Quad3_36"
73	K	J9	49.25	3	J9_Quad3_49.25"

74	K	J9	60	3	J9_Quad3_60"
75	K	J9	72	3	J9_Quad3_72"
76	K	J9	84	3	J9_Quad3_84"
77	K	J9	96	4	J9_Quad4_96"
78	K	J9	107	4	J9_Quad4_107"
79	K	J9	118.5	4	J9_Quad4_118.5"
80	K	J9	132	4	J9_Quad4_132"
81	K	J9	144	4	J9_Quad4_144"
82	K	J9	148.75	4	J9_Quad4_148.75"
83	T	J15	8	2	J15_Quad2_8"
84	T	J15	20	3	J15_Quad3_20"
85	K	J15	84	4	J15_Quad4_84"
86	K	J15	148.75	4	J15_Quad4_148.75"
87	T	J17	5	2	J17_Quad2_5"
88	T	J17	11	2	J17_Quad2_11"
89	T	J17	17	3	J17_Quad3_17"
90	T	J17	23	3	J17_Quad3_23"
91	K	J17	49.25	3	J17_Quad3_49.25"
92	K	J17	60	3	J17_Quad3_60"
93	K	J17	72	3	J17_Quad3_72"
94	K	J17	96	4	J17_Quad4_96"
95	K	J17	107	4	J17_Quad4_107"
96	K	J17	118.5	4	J17_Quad4_118.5"
97	K	J17	144	4	J17_Quad4_144"
98	T	M3	0.0	2	M3_Quad2_0.0"
99	T	M3	5	2	M3_Quad2_5"
100	T	M3	8	2	M3_Quad2_8"
101	T	M3	17	3	M3_Quad3_17"
102	T	M3	20	3	M3_Quad3_20"
103	K	M3	49.25	3	M3_Quad3_49.25"
104	K	M3	72	3	M3_Quad3_72"
105	K	M3	84	4	M3_Quad4_84"
106	K	M3	107	4	M3_Quad4_107"
107	K	M3	144	4	M3_Quad4_144"
108	K	M3	148.75	4	M3_Quad4_148.75"
109	T	M15	00	2	M15_Quad2_0.0"
110	T	M15	8	2	M15_Quad2_8"
111	T	M15	11	2	M15_Quad2_11"
112	T	M15	20	3	M15_Quad3_20"
113	T	M15	23	3	M15_Quad3_23"

114	K	M15	60	3	M15_Quad3_60"
115	K	M15	84	4	M15_Quad4_84"
116	K	M15	96	4	M15_Quad4_96"
117	K	M15	118.5	4	M15_Quad4_118.5"
118	K	M15	148.75	4	M15_Quad4_148.75"
119	T	P6	0.0	2	P6_Quad2_0.0"
120	T	P9	8	2	P9_Quad2_8"
121	T	P9	20	3	P9_Quad3_20"
122	K	P9	84	4	P9_Quad4_84"
123	K	P9	148.75	4	P9_Quad4_148.75"
124	T	P12	0.0	2	P12_Quad2_0.0"
125	T	R1	8	2	R1_Quad2_8"
126	T	R1	20	3	R1_Quad3_20"
127	K	R1	84	4	R1_Quad4_84"
128	K	R1	148.75	4	R1_Quad4_148.75"
129	T	R17	8	2	R17_Quad2_8"
130	T	R17	20	3	R17_Quad3_20"
131	K	R17	84	4	R17_Quad4_84"
132	K	R17	148.75	4	R17_Quad4_148.75"

Table A-3 List of internal (Int.) thermocouples not attached to the heater assembly.

#	Type	Surface	Location	*z* Position (in.)	Quadrant	DAQ Label
133	T	Int.	Basket	1.75	1	Basket_Q1_1.75"
134	T	Int.	Basket	14	1	Basket_Q1_14"
135	T	Int.	Basket	23	1	Basket_Q1_23"
136	K	Int.	Basket	36	1	Basket_Q1_36"
137	K	Int.	Basket	60	1	Basket_Q1_60"
138	K	Int.	Basket	132	1	Basket_Q1_132"
139	T	Int.	Basket	0.0	2	Basket_Q2_0.0"
140	T	Int.	Basket	20	2	Basket_Q2_20"
141	K	Int.	Basket	49.25	2	Basket_Q2_49.25"
142	K	Int.	Basket	72	2	Basket_Q2_72"
143	K	Int.	Basket	96	2	Basket_Q2_96"
144	K	Int.	Basket	148.75	2	Basket_Q2_148.75"
145	K	Int.	Basket	158	2	Basket_Q2_158"
146	T	Int.	Basket	1.75	3	Basket_Q3_1.75"
147	T	Int.	Basket	14	3	Basket_Q3_14"
148	T	Int.	Basket	23	3	Basket_Q3_23"
149	K	Int.	Basket	36	3	Basket_Q3_36"
150	K	Int.	Basket	60	3	Basket_Q3_60"
151	K	Int.	Basket	84	3	Basket_Q3_84"
152	K	Int.	Basket	118.5	3	Basket_Q3_118.5"
153	K	Int.	Basket	164	3	Basket_Q3_164"
154	T	Int.	Basket	0.0	4	Basket_Q4_0.0"
155	T	Int.	Basket	8	4	Basket_Q4_8"
156	K	Int.	Basket	49.25	4	Basket_Q4_49.25"
157	K	Int.	Basket	72	4	Basket_Q4_72"
158	K	Int.	Basket	107	4	Basket_Q4_107"
159	T	Int.	Basket Corner	8	1-2	Basket_Q1-2cor_8"
160	K	Int.	Basket Corner	49.25	1-2	Basket_Q1-2cor_49.25"
161	K	Int.	Basket Corner	144	1-2	Basket_Q1-2cor_144"
162	K	Int.	Basket Corner	118.5	1-4	Basket_Q1-4cor_118.5"
163	T	Int.	Basket Corner	20	2-3	Basket_Q2-3cor_20"
164	K	Int.	Basket Corner	72	2-3	Basket_Q2-3cor_72"
165	K	Int.	Basket Corner	158	2-3	Basket_Q2-3cor_158"
166	K	Int.	Basket Corner	36	3-4	Basket_Q3-4cor_36"
167	K	Int.	Basket Corner	96	3-4	Basket_Q3-4cor_96"
168	K	Int.	Top Lid	169.1	1	Top_Lid_Internal
169	T	Int.	Bottom Lid	-4.6	1	Bottom_Lid_Sump_Internal

Table A-4 List of external (Ext.) thermocouples.

#	Type	Surface	Location	z Position (in.)	Quadrant	DAQ Label
170	T	Ext.	PV	2	1	PV_Q1_2"
171	T	Ext.	PV	22	1	PV_Q1_22"
172	K	Ext.	PV	36	1	PV_Q1_36"
173	K	Ext.	PV	60	1	PV_Q1_60"
174	K	Ext.	PV	84	1	PV_Q1_84"
175	K	Ext.	PV	107	1	PV_Q1_107"
176	K	Ext.	PV	132	1	PV_Q1_132"
177	K	Ext.	PV	148.75	1	PV_Q1_148.75"
178	K	Ext.	PV	162	1	PV_Q1_164"
179	K	Ext.	PV	170	1	PV_Q1_170"
180	T	Ext.	PV	2	2	PV_Q2_2"
181	T	Ext.	PV	8	2	PV_Q2_8"
182	T	Ext.	PV	22	2	PV_Q2_22"
183	K	Ext.	PV	49.25	2	PV_Q2_49.25"
184	K	Ext.	PV	72	2	PV_Q2_72"
185	K	Ext.	PV	96	2	PV_Q2_96"
186	K	Ext.	PV	118.5	2	PV_Q2_118.5"
187	K	Ext.	PV	144	2	PV_Q2_144"
188	K	Ext.	PV	158	2	PV_Q2_158"
189	K	Ext.	PV	162	2	PV_Q2_162"
190	T	Ext.	PV	2	3	PV_Q3_2"
191	T	Ext.	PV	22	3	PV_Q3_22"
192	K	Ext.	PV	36	3	PV_Q3_36"
193	K	Ext.	PV	60	3	PV_Q3_60"
194	K	Ext.	PV	84	3	PV_Q3_84"
195	K	Ext.	PV	107	3	PV_Q3_107"
196	K	Ext.	PV	132	3	PV_Q3_132"
197	K	Ext.	PV	148.75	3	PV_Q3_148.75"
198	K	Ext.	PV	162	3	PV_Q3_162"
199	T	Ext.	PV	2	4	PV_Q4_2"
200	T	Ext.	PV	8	4	PV_Q4_8"
201	T	Ext.	PV	22	4	PV_Q4_22"
202	K	Ext.	PV	49.25	4	PV_Q4_49.25"
203	K	Ext.	PV	72	4	PV_Q4_72"
204	K	Ext.	PV	96	4	PV_Q4_96"
205	K	Ext.	PV	118.5	4	PV_Q4_118.5"
206	K	Ext.	PV	144	4	PV_Q4_144"
207	K	Ext.	PV	158	4	PV_Q4_158"

#	Type	Surface	Location	z Position (in.)	Quadrant	DAQ Label
208	K	Ext.	PV	162	4	PV_Q4_162"
209	T	Ext.	Bottom Lid	-7	N/A	Bottom_Lid_External
210	K	Ext.	Top Lid	171.5	N/A	Top_Lid_External
211	T	Ext.	TC Fitting	5	3	TC_Fitting_Q3
212	K	Ext.	Hot Feedthrough	161.8	2	Hot_Feedthrough
213	K	Ext.	Neutral Feedthrough	161.8	4	Neutral_Feedthrough
214	K	Ext.	1/4" VCR Pipe Fitting	161.8	1	1/4"_VCR_Pipe_Fitting
215	K	Ext.	Siphon Tube Fitting	161.8	1	Siphon_Tube_Fitting
216	K	Ext.	1/2" VCR Pipe Fitting	161.8	1	1/2"_VCR_Pipe_Fitting
217	K	Ext.	Mass Spec Fitting	172.4	N/A	Mass_Spec_Fitting
218	K	Ext.	Test Rod Fitting	172.4	N/A	Test_Rod_Fitting
219	K	Ext.	Weld Neck	164.625	1	Weldneck_Q1_164.625
220	K	Ext.	Weld Neck	164.625	3	Weldneck_Q3_164.625
221	K	Ext.	Weld Neck	19.5	2	Weldneck_Q2_19.5
222	K	Ext.	Weld Neck	19.5	4	Weldneck_Q4_19.5

Sandia National Laboratories